A full physics algorithm to retrieve nighttime sea surface temperature with IASI: Toward an independent homogeneous long time-series for climate studies

Virginie Capelle, Jean-Michel Hartmann, Cyril Crevoisier

A full physics algorithm to retrieve nighttime sea surface temperature with IASI: Toward an independent homogeneous long time-series for climate studies

Virginie Capelle, Jean-Michel Hartmann, Cyril Crevoisier

Laboratoire de Météorologie Dynamique/IPSL, CNRS, École polytechnique, Institut polytechnique de Paris, Sorbonne Université, École normale supérieure, PSL Research University, F-91120 Palaiseau, France.

Correspondence to: Virginie Capelle (virginie.capelle@lmd.ipsl.fr)

Abstract.
A fully physically-based algorithm is presented and used to retrieve nighttime sea-surface (skin) temperatures (SSTs) from spectra recorded by the Infrared Atmospheric Sounder Interferometer (IASI). The main advantage of the proposed approach, based on radiative transfer calculations, is to provide a dataset *totally* independent of any in-situ measurement or model. The SSTs are retrieved at the IASI spot resolution (clear sky) for the three Metop platforms, today leading to a continuous record over more than 13 years, which is planned to be extended for at least another decade. Five atmospheric transparency windows centered at 3.8, 4.0, 4.7, 9.0 and 11 μm have been used for the retrievals and the results obtained are compared with in-situ temperatures provided by the buoys network as well as with other satellite datasets. This first analysis enables to draw the following three main conclusions. First, we demonstrate the interest of using short wavelengths which lead to accurate results showing, with respect to those around 9 and 11 μm, a reduced bias thanks to significantly weaker sensitivities to errors in the modeling of the water vapor contribution to the atmospheric absorption and emission. Second, we show that the observed dependences of the skin-bulk temperature difference on various observed-scene parameters (wind speed, air-sea temperature difference, humidity) are consistent with predictions of theoretical and empirical models, as well as with those from other SST products. Finally, the overall averaged bias between our retrieved values converted to bulk temperatures and those provided by in-situ measurements is -0.04 K (median: -0.024 K), with a standard deviation (SD) of 0.38 K (Robust SD=0.25 K). The bias is thus well below the 0.1 K required for a SST product usable for climate studies and extremely stable over more than a decade. Then, we investigate the consistency between the three generations of IASI on-board Metop-A, -B, and -C over their overlap periods (2013-2020 for Metop-A and Metop-B, and 2019-2020 for Metop-C) by comparing the associated retrieved monthly-averaged SSTs over 1°x1° grids. The mean differences obtained are lower than 0.02 K, with a SD of 0.3 K consistent with the natural variation of the SST within a month. This demonstrates the high stability of the SSTs retrieved using spectra recorded from the IASI suite and opens the possibility to access to long time series for climate studies. This is tested in a preliminary investigation of the SST anomalies between 2008 and 2020, with the successfully detection of short-term (El Nino and La Nina) changes as well as of a global warming trend of about +0.3 K/decade quantitatively consistent with other observations.

Keywords :
* Sea surface skin temperature
* Infrared Radiative transfer retrieval algorithm
* Infrared Atmospheric Sounder Interferometer (IASI)
* Long time series

Highlights:

- Fully physically-based algorithm to retrieve SSTs from infrared hyperspectral sounders
- A consistent and independent SSTskin time series retrieved from IASI
- Results are accurate enough for climate studies

1. Introduction

The sea surface (skin) temperature (SST) is a key parameter in climate science, meteorology and oceanography. Being at the ocean-atmosphere interface, it plays a crucial role in the variability and regulation of climate and its knowledge is essential to understand heat, momentum and gases exchange processes between the ocean and the atmosphere. As such, it is recognized as one of the essential variables (Bojinski et al., 2014) for which accurate and global measurements are needed for the understanding, monitoring and forecasting of climate evolution, as well as for numerical weather predictions. From this point of view, satellite-based instruments are particularly well adapted, since they can be used for the remote sensing of daily and spatially-global data over long time scales. Since the early 1980s, an increasing number of sensors of high radiometric quality provide regular SST estimations through observations in different viewing configurations. These include low-Earth and geostationary orbiters, with soundings in the infrared or microwave spectral domains, each of them offering different advantages and drawbacks (see e.g. Minnett et al., 2019; O'Carroll et al., 2019). Recall that SST determinations for climate studies are very challenging since they should fulfill several demanding constraints. (i) First, since one must be able to detect trends, with changes lower than 0.2 K/decade, the accuracy of the retrieved SST should be better than 0.1 K with a stability better than 0.05 K/decade (Ohring et al., 2005; Merchant et al., 2008; Minnett and Corlett, 2012). (ii) Second, climate analysis requires time series with at least 15 years of homogeneous observations, a period often exceeding the lifetime of a specific instrument. Data collected by several sensors must thus be combined, which raises the challenging issue of maintaining the consistency over years and avoiding discontinuities at each change of instrument. Some adjustments are consequently required to reconcile the calibrations of the different experiments. For example, the data provided by the (Advanced) Along-Track Scanning Radiometers [(A)ATSRs] series (Merchant et al., 2012; Veal et al., 2013) were harmonized by using the most recent instrument as a reference and by applying corrections to the brightness temperatures provided by the older ones taking advantage of the partial time overlapping of the series. Recall that a bias of 0.2 K was observed between SSTs derived from ATSR-2 and AATSR before this procedure was applied. More recently, a satellite time-series of SSTs was produced, from 1981 to 2016, by merging observations from the three ATSRs with those of eleven Advanced Very High Resolution Radiometers (AVHRRs) (Merchant et al., 2019). The data from AATSR were used as the reference to recalibrate those provided by the other sensors at 3.7 and 11 µm, while ATSR-2 recordings were retained for re-calibrations at 12 µm, given an identified anomalous offset of up to 0.3 K on AATSR. (iii) Third, remotely sensed SST time series should be as little dependent as possible from any other data (in-situ measurements, models, etc…). This is crucial to confirm (or not) any trend or variation observed in one specific set of data (Ohring et al., 2005; Merchant et al., 2012). The independency from in-situ measurements is also of interest because the latter then enable the validation of the considered SST datasets. However, relatively few fully independent records are available since many retrieval algorithms are based on regressions from in-situ data, as done, for instance, to generate the AVHRR (Kilpatrick and Baker-Yeboah, 2016) and MODIS (Kilpatrick et al., 2015) SST databases. A notable exception is the ATSR Reprocessing for Climate (ARC) project (Merchant et al., 2012), which is based

on a radiative transfer model providing a high [but not full since the cloud filtering is based on numerical weather prediction (NWP) models that include in-situ and satellite SST measurements] independence from in-situ measurements. (iv) Finally, an important requirement for the reliability of SST retrievals is to achieve the highest possible sensitivity to surface temperature changes (Minnett et al., 2019) together with the lowest dependence on the other parameters describing the observation scene. For example, it has been demonstrated that several algorithms suffer from sensitivity to the humidity profile, in particular for tropical regions where the absorption by atmospheric water vapor attenuates the sensitivity to surface temperature variations. Indeed, (Merchant et al., 2009) determined for the AVHRR SST product of the Pathfinder project (Kilpatrick et al., 2001) that the sensitivity to a surface temperature change can be reduced down to 0.5 $K.K^{-1}$ in extreme cases (i.e the variation of the retrieved SST is 0.5 K for an actual variation of 1 K).

Within this context, the Infrared Atmospheric Sounding Interferometer (IASI) instrument (Hilton et al., 2012) can provide a valuable contribution to long-term SST studies thanks to: (1) its well-specified calibration (Blumstein et al., 2004) based on two internal blackbody targets and two cold space views made for every scan along the IASI track; (2) the exceptional stability of both the spectral and radiometric calibrations which makes this instrument the current reference for the first operational Global Space-based Inter-Calibration System (GSICS; http://gsics.wmo.int/) product, namely, the inter-calibration corrections for infrared channels of Meteosat/SEVIRI (Hewison et al., 2013); (3) the planned long time series of 20 years of observations provided by the suite of three satellites Metop-A, -B and -C, launched respectively in October 2006, September 2012 and November 2018. Currently, EUMETSAT delivers an operational IASI SST product (August et al., 2012; O'Carroll et al., 2012) in which the SST is retrieved using linear regressions on the basis of empirical orthogonal functions using principal components of the radiances from bands 1 (645.00-1210.00 cm^{-1}) and 2 (1210.00-2000.00 cm^{-1}). A cloud filtering partly based on comparison with NWP products is used. So far, the time series has never been reprocessed and suffers from an inhomogeneity due to successive changes in the retrieval algorithms. It therefore cannot be used 'as is' in climate analyses.

In this study, we propose a method for the restitution of accurate and independent nighttime sea surface skin temperatures from the three IASI instruments on the successive Metop platforms, based on a full physics algorithm. In our approach, SSTs are retrieved using *only* the observed IASI brightness temperatures, and they are derived through radiative transfer modeling from the Thermodynamic Initial Guess Retrieval (TIGR) database (Chedin et al., 1985; Chevallier et al., 1998), without use of any a priori. Moreover, clear-sky conditions are selected, based only on IASI and co-registered AVHRR observations used to infer the homogeneity of the scene within the IASI fields of view. The SST time series obtained, spanning more than 13 years so far, is thus *fully* homogeneous and totally *free* of any use of other SST products. This enables a precise and independent validation through in-situ measurements from the drifting buoys network.

The remainder of this paper is organized as follow: The methodology used to retrieve SSTs from IASI radiances is describes in Sec. 2. The values obtained are then compared to drifting buoys measurements in Sec. 3, providing an independent and successful validation, while Sec. 4 focuses on the consistency between the results retrieved from observations of the three IASI instruments on-board the Metop satellites.

2. Retrieving sea surface temperature from IASI

2.1. The IASI instrument

The Infrared Atmospheric Sounding Interferometer (IASI), is a satellite-based Fourier transform spectrometer that records the infrared radiation emitted by the earth (Blumstein et al., 2004). It provides radiances at 8461 spectral points, from 645.00 to 2760.00 cm^{-1} (15.5 to 3.63 µm) with a step of 0.25 cm^{-1} and a spectral resolution of 0.50 cm^{-1} after apodization (for the Level-1c spectra used here). The instantaneous field of view (IFOV) has a ground resolution of 12 km at nadir over a swath width of about 2200 km (+/-50°). IASI is flying onboard the Metop-A, -B, and -C series of polar-orbiting meteorological satellites. Metop-A was launched in October 2006 and the associated Level-1c data, available since July 2007, are routinely downloaded via the "atmosphere and service data Pole" AERIS (https://en.aeris-data.fr/), through the Broadcast System for Environmental Data of EUMETSAT (EUMETCast). Metop-B was launched in September 2012 (Level-1c data available since February 2013). Metop-A and B operated in a co-planar orbit, 180 degrees out of phase until the launch of Metop-C, in November 2018 (Level-1c data available since July 2019). During the commissioning phase, the three Metops were phasing with 120 degrees separation, Metop-C at equal distance from Metop-A and Metop-B ("Tristar configuration", see e.g. https://www.eumetsat.int/preparing-for-metop-c-data). Since February 2020, the three satellites fly in "Trident phasing" with Metop-B and Metop-C flying with a 180 degrees opposition (i.e., the former Metop-A/Metop-B configuration) and Metop-A approximately 90 degrees in-between. All three satellites have a local time of ascending node of 21:30 (+/-15 mn). Note that the last inclination correction to the Metop-A platform having been made in August 2016 in order to maximize the satellite lifetime, the local time of the equator crossing is since then changing (Dyer et al., 2018), with a cumulated drift of about -42 mn in March 2020.

IASI L1c data are provided together with information from the Advanced Very-High-Resolution Radiometer (AVHRR) co-registered pixels. Several of those within a IASI IFOV are combined in a maximum of 7 homogeneous clusters for which the mean radiance and associated standard deviation are given for each IASI pixel. This brings information on the observed scene homogeneity, which is useful to detect the eventual presence of clouds.

2.2. General approach

The sea surface skin temperature, T_{Skin}, is retrieved using a fast radiative transfer model. For clear-sky nighttime conditions, under the assumption of local thermodynamic equilibrium and considering the reflection of the downward flux at the sea surface as isotropic, the radiative transfer equation may be approximated using a monochromatic simplification (e.g. Turner, 2004) and the radiance I_{sat} received by the instrument can be expressed, for each wavelength λ and viewing angle θ, as:

$$I_{sat}(\lambda,\theta) = \varepsilon_s(\lambda,\theta)\langle\tau_s(\lambda,\theta)\rangle B(\lambda,T_{Skin}) + \sum_{k=1\ (satellite)}^{N\ (surface)} B(\lambda,T_k)[\langle\tau_k(\lambda,\theta)\rangle - \langle\tau_{k+1}(\lambda,\theta)\rangle] + \big(1-\varepsilon_s(\lambda,\theta)\big)\langle\tau_s(\lambda,\theta)\rangle \sum_{k=1\ (satellite)}^{N(surface)} B(\lambda,T_k)\,[\langle\tau'_k(\lambda)\rangle - \langle\tau'_{k+1}(\lambda)\rangle]. \quad (1)$$

where the subscript s denotes the surface, τ_k is the spectral value of transmission of the line-of-sight between a given level k of the atmosphere and the satellite, τ_s is the transmission between

the surface and the satellite, and τ'_k denotes the transmission between level k and the surface under the incident angle 53°. ε_s is the directional emissivity of the sea surface, and $B(\lambda,T)$ is the Planck function value at wavelength λ for a temperature T. $\langle f(\lambda)\rangle$ means that the function $f(\lambda)$ has been convoluted by the instrument response function. Note that only the transmissions need to be convoluted, since the other quantities are either independent of the wavelength or can be considered as constant within the spectral extent of the IASI instrument function. Equation (1) can easily be inverted in order to obtain the surface temperature T_{Skin}, leading to:

$$T_{skin} = B^{-1}\left(\left[I_{sat}(\lambda,\theta) - \sum_{k=1(satellite)}^{N\,(surface)} B(\lambda,T_k)[\langle\tau_k(\lambda,\theta)\rangle - \langle\tau_{k+1}(\lambda,\theta)\rangle] - (1-\varepsilon_s)\langle\tau_s(\lambda,\theta)\rangle \sum_{k=1(satellite)}^{N\,(surface)} B(\lambda,T_k)\,[\langle\tau'_k(\lambda)\rangle - \langle\tau'_{k+1}(\lambda)\rangle]\right] / \varepsilon_s(\lambda,\theta)\langle\tau_s(\lambda,\theta)\rangle\right)$$

. (2)

Tshe ocean surface emissivity ε_s is relatively well known, in particular for observations close to nadir ($|\theta|<30°$) where it depends principally on the refractive index of sea water and, to the second order, on θ (Masuda et al., 1988). Furthermore, Masuda et al. (1988) showed that, for such viewing angles, the wind speed has a very small influence on ε_s which was therefore neglected in this study. The surface temperature T_{Skin} can thus be accurately obtained if the transmissions (τ_s, τ_k and τ'_k) and the local atmospheric emissions $B(\lambda,T_k)$ are known. When the thermodynamic state of the atmosphere is specified (a minima the temperature, total pressure and water vapor profiles if the spectral channels retained are adequately selected, see below), the transmissions in Eq. (2) can be computed using a radiative transfer model. Note that, in an ideal situation, when the observed atmosphere is perfectly characterized and the transmissions are exactly predicted (implying no error in the spectroscopic data and radiative transfer calculation), all spectral channels λ_i would provide identical values of T_{Skin}. In practice, for a given wavelength, the lower $\tau_s(\lambda_i,\theta)$ is, the more sensitive it is to errors in the atmospheric state knowledge and spectroscopic data used with, consequently, an increased impact on the retrieved SST. This shows that the selection of the spectral points used for the retrieval is a key issue.

2.3. Channels selection

A set of channels λ_i presenting high surface-to-space atmospheric transmissions $\tau_s(\lambda_i)$ were first selected throughout the entire IASI spectral range. Those retained were chosen in between absorption lines, at spectral points of locally minimum absorption where $\tau_s(\lambda_i,\theta=0)$ is greater than 0.55. Figure 1, which displays the transmission $\tau_s(\lambda_i,\theta)$ calculated for a nadir-view ($\theta=0°$) and a typical tropical atmosphere with a total precipitable water (TPW) content of 3.8 cm, also points out the 462 channels used in this study. The latter are spread within five spectral windows centered near 11.0 μm (70 channels), 9.0 μm (68 channels), 4.7 μm (32 channels), 4.0 μm (107

channels) and 3.8 µm (185 channels). Note that the points around 11 µm, being those where the transmission is the lowest, are the most sensitive to the atmospheric absorption. Together with local H_2O spectral lines, the water vapor continuum (Mlawer et al., 2012) here makes the largest contribution, implying that both this continuum and the humidity profile must be precisely known for accurate SST retrievals using this spectral region. The window around 9 µm involves slightly higher transmissions which however remain significantly dependent on the atmospheric contribution and, again, on the water vapor continuum. Despite these disadvantages, the 9 and 11 µm windows are however interesting since the instrumental noise of IASI is here relatively low (<0.2 K). Around 4.7 µm, the transmissions are generally greater than 0.7 with values for some of the channels that are above 0.85. This region is also less sensitive than long wavelengths to the water vapor continuum and moderately affected by instrumental noise. The same remarks apply to the 4 µm window, with transmissions generally above 0.8 and locally greater than 0.9. Note that, as shown in (Hartmann et al., 2018), one must here take the influence of humidity on the N_2 and CO_2 contributions to the spectra into account, since this can reduces the difference between simulated and observed brightness temperatures by up to 0.4 K for very humid atmospheres. Finally, the highest frequency window (around 3.8 µm) is that where both the atmospheric transmission and the relative sensitivity to the SST [i.e. $\mathrm{d}B(\lambda,T_{\mathrm{Skin}})/\mathrm{d}T_{\mathrm{Skin}}|/B(\lambda,T_{\mathrm{Skin}})$] are the highest, but also where the IASI spectra carry the largest radiometric noise (between 0.8 and 1.8 K for a typical tropical atmosphere). However, by selecting a high number of spectral channels (185), the noise in this spectral region is reduced by more than 13, leading to an overall noise equivalent lower than 0.1 K. This preliminary analysis, confirmed latter and in Appendices A1 and A2, indicates that the short wavelengths are likely more adapted that the longest ones for precise SST retrievals.

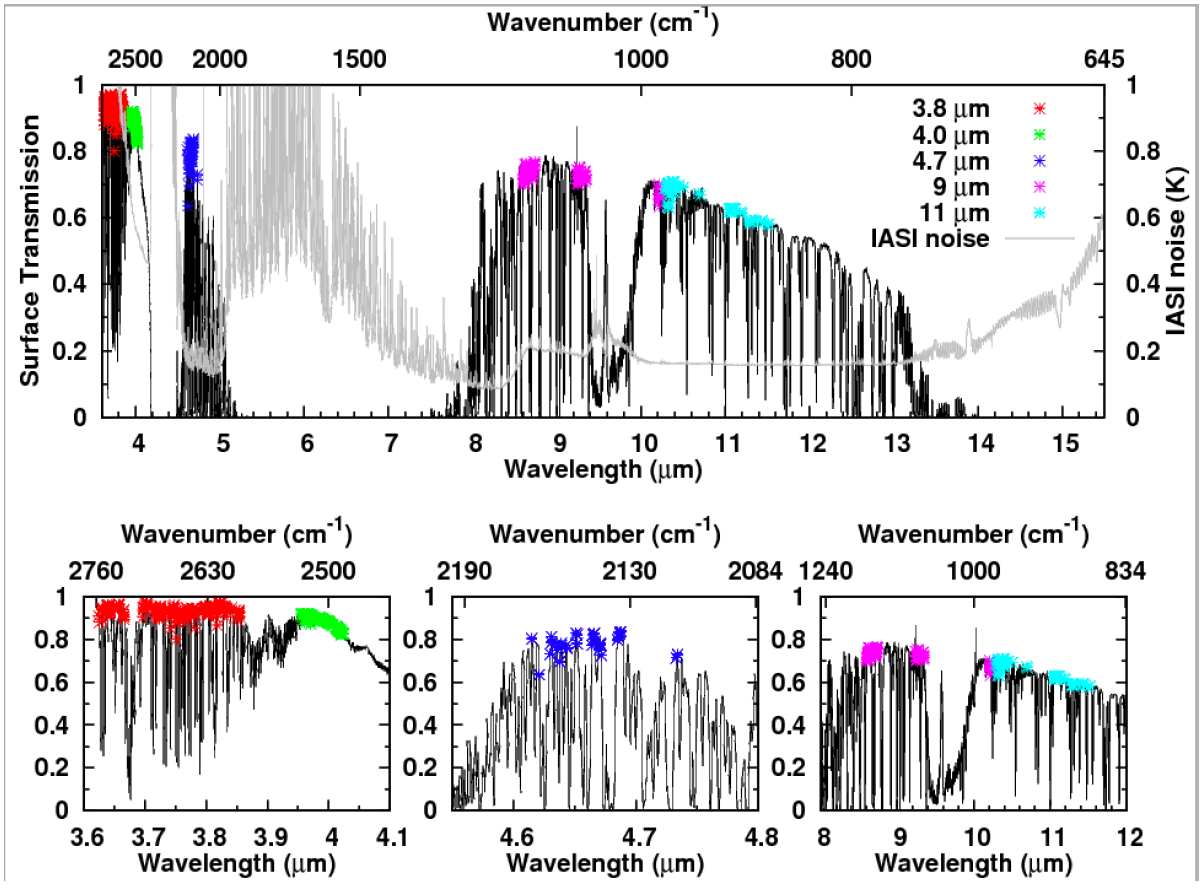

Figure 1: Surface-to-space computed vertical transmission for a typical tropical atmosphere (TPW = 3.8 cm), black line, and instrumental radiometric noise, light grey line, in terms of the Level-1c noise-equivalent brightness temperature

expressed at the wavelength dependent value of the scene brightness temperature. The symbols indicate the 462 channels selected for this study, each color corresponding to a different "transparency" window. The entire IASI spectral range is displayed in the top panel, the lower ones providing zooms on specific regions.

2.4. Cloud/dust filtering

It is well known that infrared radiances collected from space are very sensitive to the presence of clouds which can reduce the observed brightness by up to several dozen degrees. If not properly taken into account, this can lead to largely underestimated values of the retrieved SST. For this reason, and since the main objective of this study is to assess the capability of IASI to provide precise SSTs, a strict cloud (and dust) filtering was first applied, using a procedure that is *independent* of any external meteorological model or data. In contrast, in the IASI level 2 product, for example, cloud detection is based, among others, on comparisons between the observed IASI radiances and those simulated using the NWP fields of temperature, humidity, ozone, surface temperature and surface pressure provided by ECMWF (see e.g "IASI L2 PPF v6 _ 3 - Validation Report", EUM/RSP/REP/17/920559 on https://www.eumetsat.int/ website), which assimilate buoys temperature data. In order to perform a meaningful (and thus independent) validation of our retrieved SSTs by comparisons with drifting buoys in-situ measurements, we therefore cannot use the L2 cloud detection. For this reason, four successive tests were applied, based *only* on the IASI radiances.

- *Test1*: Only those IASI spectra for which the SST retrieved at 3.8 µm is greater than 273 K were kept. Below this threshold, either the probed sea surface is (partly) ice, and the emissivity used is no more valid, or a cloud is present.
- *Test 2*: For each IASI spectrum, we compare the brightness temperature (BT) at 4.7 µm (2143.25 cm^{-1}) with the BT at 3.8 µm obtained, in order to reduce the impact of the radiometric noise in this region, by averaging the BTs of all retained channels within this window. Since the atmosphere is less transparent at 4.7 µm than near 3.8 µm (see Fig. 1), one should have BT(3.8 µm)>BT(4.7 µm). According to this, a IASI spectrum is rejected when the (very) conservative criterion BT(3.8µm)-BT(4.7µm)>-0.2 K is not satisfied.
- *Test 3*: The BT at 2143.25 cm^{-1} for the considered observed pixel is compared to the largest BT, for the same wavenumber, of the neighboring pixels along the cross scan line (limited to +/-20° changes of the zenith angle). Only those spectra for which BT>0.99*max[BT(+/-20°)], which corresponds to a BT variation around 3 K, were kept. Given the sensitivity of the 2143.25 cm^{-1} channel to the atmospheric state, this threshold corresponds to a change of the atmospheric temperature profile by more than 10 K, or of the water profile by more than 200 %, much above the natural spatial variations associated with a +/-20° change of θ for clear sky conditions.
- *Test 4*: The radiance variability among the AVHRR clusters collocated with the IASI pixel is considered as a proxy for the presence of dispersed clouds. It is here quantified by calculating the mean differences, in BT, of the 3.7 µm AVHRR channel 3b within each AVHRR cluster. Choosing a low threshold improves the standard deviation between retrieved SSTs and in-situ temperature measurements but this simultaneously significantly reduces the number of collocations. A value of 0.5 K, which provides a good compromise, was empirically chosen.
- *Test 5*: The dust-contaminated observations potentially remaining after applying the above described four tests are removed after retrieving the dust optical depth (DAOD) at 10 µm by using the method described in (Capelle et al., 2018). All IASI spectra with a DAOD>0.03 are eliminated.

Altogether, these different tests lead to the rejection of about 94% of the IASI observations.

2.5. SST retrieval methodology

The algorithm applied to retrieve the SST is based on the method described in (Péquignot et al., 2008; Capelle et al., 2012). Transmissions profiles are computed once and for all with the 4A/OP code (Scott and Chédin, 1981, available on https://4aop.aeris-data.fr) for all the

atmospheric situations archived in the TIGR database (Chedin et al., 1985; Chevallier et al., 1998) and for 13 viewing angles between 0° and 53°. For this, the spectroscopic line parameters were taken from the GEISA 2015 database (Jacquinet-Husson et al., 2016), complemented by the MT-CKD 3.2 parameterization (Mlawer et al., 2012) of the water vapor continuum. The contributions of the collision-induced absorption by N_2 and of the wings of the CO_2 lines, both around 4 μm, were computed as described in (Hartmann et al., 2018).

For each IASI observation, as in (Capelle et al., 2012), the thermodynamic state of the atmosphere was determined, in a first step, using a proximity recognition within the TIGR database for a selection of 8 channels principally sensitive to the temperature and water profiles with relatively small contributions from other gases and from the surface. In a second step, using the associated precomputed transmission profiles, wavelength-dependent values $T_{Skin}(\lambda_i)$ of the SST are retrieved using Eq. (2) for the selected channels λ_i described above. Then the results obtained within each of the five spectral regions are averaged, providing SSTs at 11.0, 9.0, 4.7, 4.0, and 3.8 μm.

The sensitivities of the retrieved SST to the water and temperature profiles and to the surface emissivity for each spectral region are studied in Appendix A1 which shows how the retrieved SST varies for a given change of each parameter. This helps quantifying how an error made on the atmospheric profile or on the surface emissivity biases the retrieved SST according to the spectral region used. This exercise confirms that long wavelengths are significantly more sensitive to errors in the input atmospheric temperature and humidity profiles, particularly for large TPW values. For instance, for TPW=3 cm, a +10 % change of the water vapor amount increases the SST retrieved at 11 μm by about +0.7 K while that retrieved at 3.8 μm changes by only 0.05 K, with corresponding values of -0.5 K and -0.05 K for a +1 K increase of the temperature profile. Long wavelengths are also, but to a lesser extent, more sensitive to a change of the sea surface emissivity (-0.04 K and -0.02 K at 11.0 and 3.8 μm, respectively, for a TPW of 3 cm and a +0.001 change of the emissivity). Appendix A2 further discusses the effect of humidity by considering the sensitivity of the retrieved SST to the water vapor self and foreign continua (Mlawer et al., 2012). Again, SSTs retrieved using long wavelengths are significantly more affected that short ones by errors in the spectroscopic knowledge of these continua. For instance, for a TPW of 3 cm, a 10% increase of the self-continuum changes the SST retrieved at 11 μm by +0.3 K while the effect at 3.8 μm is below 0.01 K.

3. Validation of IASI retrieved SST

3.1. Validation with *i*Quam in-situ measured bulk temperatures

3.1.1 In-situ data used

The SST retrieved from infrared satellite observations corresponds to the temperature of the thermal skin layer of the ocean, at a depth of about 10-20 μm. The ideal method to validate such restitutions is to use data obtained from measurements of the radiance emitted by the sea surface collected by ship-mounted infrared radiometers. Such datasets do exist (Donlon et al., 2008; Minnett et al., 2001, 2011), but they only cover very short periods of time and very limited areas. For the broad time scale (2008-2020) of the IASI observations analyzed in this study, the possible comparisons with collocated ship measurements made at the same place and time and under clear sky conditions are too few and sparse to enable any meaningful statistical analysis. The skin SSTs T_{Skin} retrieved from IASI will therefore be compared in the following to the temperatures measured from buoys significantly below the thermal skin layer (a few centimeters or more under the air-sea interface), from now on denoted as bulk temperatures (T_{Bulk}). Here, the archive from the NOAA in-situ Quality Monitor (*i*Quam; www.star.nesdis.noaa.gov/sod/sst/iQuam/)) (Xu and Ignatov, 2014) is used. This project

follows three main objectives in near real time: (i) To perform quality control of the in-situ bulk temperatures collected from different types of platform (drifters, ships, and tropical and coastal moorings). (ii) To monitor quality-controlled T_{Bulk} values online. (iii) To distribute in-situ bulk temperature data with quality level and flags appended. Note that *i*Quam provides data from September 1981 up to now, with very good spatial and temporal coverages.

3.1.2 T_{Skin} versus T_{Bulk} comparisons

The in-situ bulk temperatures, T_{Bulk}, archived in *i*Quam, being representative of the uppermost few meters of the ocean, are different from the skin surface temperatures T_{Skin} retrieved from satellite spectra. The difference $\Delta T=T_{Skin}-T_{Bulk}$ is not easy to predict accurately because it depends on the thermal gradient within the first millimeters below the sea surface (e.g. Saunders, 1967) and on the heat at mass exchanges occurring at the ocean-atmospheric interface. Simple but strictly empirical laws have been proposed in which ΔT is parameterized as a function of the wind speed only (Donlon et al., 2002; Horrocks et al., 2003; Minnett et al., 2011; Alappattu et al., 2017; Zhang et al., 2020). More elaborated models also involve the air humidity and temperature and the net long-wave radiative flux (e.g. Schluessel et al., 1990). Other more complex and physically-based theoretical descriptions are also available, in which ΔT depends on the net flux and the viscous stress at the surface due to wind, as well as on either on the thickness (Saunders, 1967; Fairall et al., 1996; Zhang and Zhang, 2012) or the renewal characteristic time (Liu et al., 1979; Soloviev and Schlüssel, 1994; Castro et al., 2003) of the thermal skin layer. Analysis of the literature shows that, while most models due capture some trends of ΔT (e.g. the increase of the nighttime $|\Delta T|$ with increasing net flux and its decrease with increasing wind speed), they poorly reproduce its variability [see e.g. Fig. 2 of (Emery et al., 2001)].

3.1.3 Collocation procedure

Based on the error characterization of the different in-situ platform types performed in (Xu and Ignatov, 2016), only measurements of T_{Bulk} from drifters, which have the best accuracy, have been retained. For the latter, Xu and Ignatov (2016) estimated a standard deviation for nighttime conditions around 0.21 K, using triple-collocation analyses. Any measurement in the *i*Quam database for which the highest quality flag (quality level QL=5) is not reached was disregarded in the present study. Finally, to avoid remaining outliers that would have passed this quality control, an additional filtering is made, which rejects the data if the difference between the measured T_{Bulk} and the global 0.25° daily analysis reference Reynolds optimal interpolation SST (Reynolds et al., 2007) is larger than 5 K. Clear sky IASI observations collected from both Metop-A and B have then been collocated with drifting buoys, selected for a maximum distance of 20 km and a maximum time shift of +/-3 h. For each in-situ datum, the closest clear-sky near nadir ($|\theta|<30°$) IASI observation meeting these criteria was retained and skin surface temperatures were retrieved using the method described in section 2, leading to about 1500 observations a month per instrument.

3.2 Overall statistics between IASI SSTs and in-situ measured temperatures

Sea surface temperatures, T_{Skin}, retrieved from IASI in the five spectral regions defined in Sec. 2.3 have first been directly compared with the associated in-situ measurements, T_{Bulk}, for all the clear sky Metop-A/buoys collocations for the year 2016. Note that, starting from 311639 collocations, applying the cloud filtering described in Sec. 2.4 reduces their number by about 95%, down to 16411.

Table 1: Differences $\Delta T=T_{Skin}-T_{Bulk}$ between the IASI/Metop-A-retrieved SST (T_{Skin}) and the in-situ-measured bulk temperature (T_{Bulk}) for all the clear-sky collocations of the year 2016. Statistics are given for the five spectral regions in terms of the mean (mean) and the standard deviation (SD), as well as using "robust statistics" (med and RSD) which

are more appropriate when analyzing non-normal distributions, for example in presence of outliers. Are also given the number of collocations involved and the percentage of collocations that were retained among all those available.

Nb colloc.	% from origin		11. µm		9.0 µm		4.7 µm		4.0 µm		3.8 µm	
16411	5.3	mean/SD	-0.42	0.61	-0.44	0.48	-0.29	0.41	-0.25	0.39	-0.27	0.39
		med/RSD	-0.36	0.43	-0.40	0.34	-0.26	0.28	-0.23	0.25	-0.25	0.25

Table 1 displays the statistics obtained for $\Delta T = T_{Skin} - T_{Bulk}$, as given by the mean and the standard deviation as well as using "robust statistics" which use the median (med) instead of the mean (mean) while the standard deviation (SD) is replaced by the robust standard deviation (RSD) defined as 1.5 times the Median Absolute Deviation, i.e. the deviation from the absolute median (e.g. Rousseeuw and Hubert, 2011). For the SSTs retrieved at 4.7 µm, 4.0 µm and 3.8 µm, the difference between mean and median is smaller than 0.02 K, whereas the standard deviation is more affected, with a difference SD-RSD of about 0.15 K. This implies that outliers, here mostly due to "extreme" situations, such as those where residual clouds are present, represent few items in the distribution, but with large biases. For example, the collocations for which the value of $|\Delta T|$ obtained at 3.8 µm is larger than 2 K represent about 0.25% of the ensemble. If they are removed, the mean ΔT (standard deviation) changes from -0.27 K (0.39 K) to -0.26 K (0.31 K).

Table 1 shows that the SSTs retrieved at 4.7, 4.0 and 3.8 µm are very consistent. The median ΔTs are around -0.25 K with RSDs of 0.25 K for the two shortest wavelengths. The RSD is slightly larger for 4.7 µm (+0.03 K), consistent with the above-mentioned higher sensitivity of this spectral region to the atmospheric state (see Sec. 2.3 and Appendix A1). Strengthening the cloud filtering (Sec. 2.4) by increasing the BT/BTmax threshold (Test 3, 0.995 instead of 0.990), lowering the AVHRR variability threshold (Test 4, from 0.5 K to 0.2 K or 0.1 K), or decreasing the AOD threshold (Test 5, from 0.03 to 0.01) largely reduces the number of collocations without significantly changing the mean ΔT and standard deviation. At 11 µm (and to a lesser extent at 9 µm), the RSD is significantly larger than at the shorter wavelengths, increased by about +0.2 K at 11 µm and +0.1 K at 9 µm, with an increase of around +0.1 K for the median $|\Delta T|$. These two spectral regions suffer, as mentioned above, from a stronger sensitivity to the atmospheric state which explains the higher SDs and RSDs. The standard deviations (0.39 K), as well as the RSDs (0.25 K), obtained for the two shortest wavelengths are comparable with values often cited for other satellite estimations such as those from MODIS (Kilpatrick et al., 2015), AATSR (Tsamalis and Saunders, 2018 ; Zhang et al., 2019), and IASI (O'Carroll et al., 2012). Note that for AATSR, some studies provide a RSD below 0.2 K (O'Carroll et al., 2008; Merchant et al., 2012; Embury et al., 2019) [See also (Minnett et al., 2019) for a detailed review of satellite-based SST determinations]. Let us emphasize that the RSDs obtained here are close to the uncertainty of about 0.21 K estimated for the in-situ bulk temperature measurements (Xu and Ignatov, 2016), demonstrating the quality of the present IASI SST restitutions. It should, in particular, be noted that, despite the relatively high radiometric noise of IASI radiances below 4 µm, the associated standard deviations obtained on ΔT are small, demonstrating the usefulness of the short wavelengths for accurate SST retrievals. This is achieved thanks to the simultaneous use of 185 channels around 3.8 µm and 107 around 4.0 µm (see Fig. 1), which enables to significantly reduce the impact of random measurement errors. The obtained median (-0.25 K) is globally consistent with the so-called "cool skin effect" caused by the combined influences of net longwave radiation, sensible and latent heat fluxes, which was shown to lie between -0.1 and -0.5 K (e.g., Saunders, 1967; Fairall et al., 1996). It is slightly larger than the average value (around -0.2 K) generally obtained from

shipboard measurements (Donlon et al., 2002; Minnett et al., 2011), but it is consistent with the CASPER-East experiment (Alappattu et al., 2017) which yielded ΔT=-0.4 +/-0.2 K.

In order to go further in the validation of the retrieved SSTs, the next section investigates the dependence of the ΔTs on various characteristics of the observed scenes. This is done using clear-sky Metop-A/buoys collocations for the year 2016 by considering the influences of the humidity, wind speed and air-sea temperature difference, which are analyzed through comparisons with empirical or theoretical models of the cool-skin effect as well as with other SST products.

3.3 Sensitivity to the observed scene conditions and comparisons with other SST products

In this section, comparisons between retrieved skin temperatures and in-situ bulk temperatures are analyzed using robust statistics (median and robust standard deviation), in which outliers are not removed but where their impact on the statistics is attenuated, and we focus on the clear-sky collocations with Metop-A in 2016 (16411 collocations). The dependences of the ΔTs to the local conditions are compared to other satellite-based determinations, as well as to the theoretical parametrization of Fairall et al. (1996), hereafter denoted FA96. In the latter, which is based on the previous work of Saunders (1967), ΔT is assumed to be governed by forced convection in a cool skin layer of thickness δ, except for low wind conditions where free convective losses dominate. ΔT then depends on the net heat flux Q at the surface, defined as $Q=R_{nl}+H_s+H_l$ (where R_{nl} denotes the net longwave radiation, H_s the sensible heat flux and H_l the latent heat flux), as well as on the friction velocity (u_{*a}). Equations (13) and (14) of Fa96 were used, with input values of R_{nl}, H_s, H_l and u_{*a} provided by the European Centre for Medium-Range Weather Forecasts (ECMWF) model ERA5 forecast data (Hersbach et al., 2018,2020), and the needed temperature-dependent sea-water thermophysical properties were taken from web.mit.edu/seawater (Sharqawy et al., 2010; Nayar et al., 2016). It should be emphasized that if the comparison between measured and calculated ΔTs may help to assess the reliability of the obtained variations of ΔT, this cannot be considered as an absolute validation given that 1) the FA96 parametrization is not exact and 2) the heat fluxes and the other variables required for this estimate are taken from a forecast model and not from direct in-situ measurements.

3.3.1 Influence of the Total Precipitable Water (TPW) content

As is well known and was mentioned above, the main difficulty when retrieving SSTs from infrared sounders spectra is to accurately take the atmospheric absorption and emission contributions into account. This is particularly challenging for the 9 and 11 μm windows which are significantly (and the most) sensitive to the atmospheric humidity (see Appendix A1). At these long wavelengths, use of an incorrect water vapor profile (not to mention the spectroscopic issue and particularly that associated with the water vapor continuum, see Appendix A2) can lead to significant errors in the retrieved SST, as previously observed for MODIS and AATSR restitutions (Embury et al., 2012; Kilpatrick et al., 2015; Zhang et al., 2019). Analyzing the variation of ΔT with the total precipitable water (TPW) content is therefore useful to identify the potential "atmospheric (or spectroscopic) contamination" of the retrieved values.

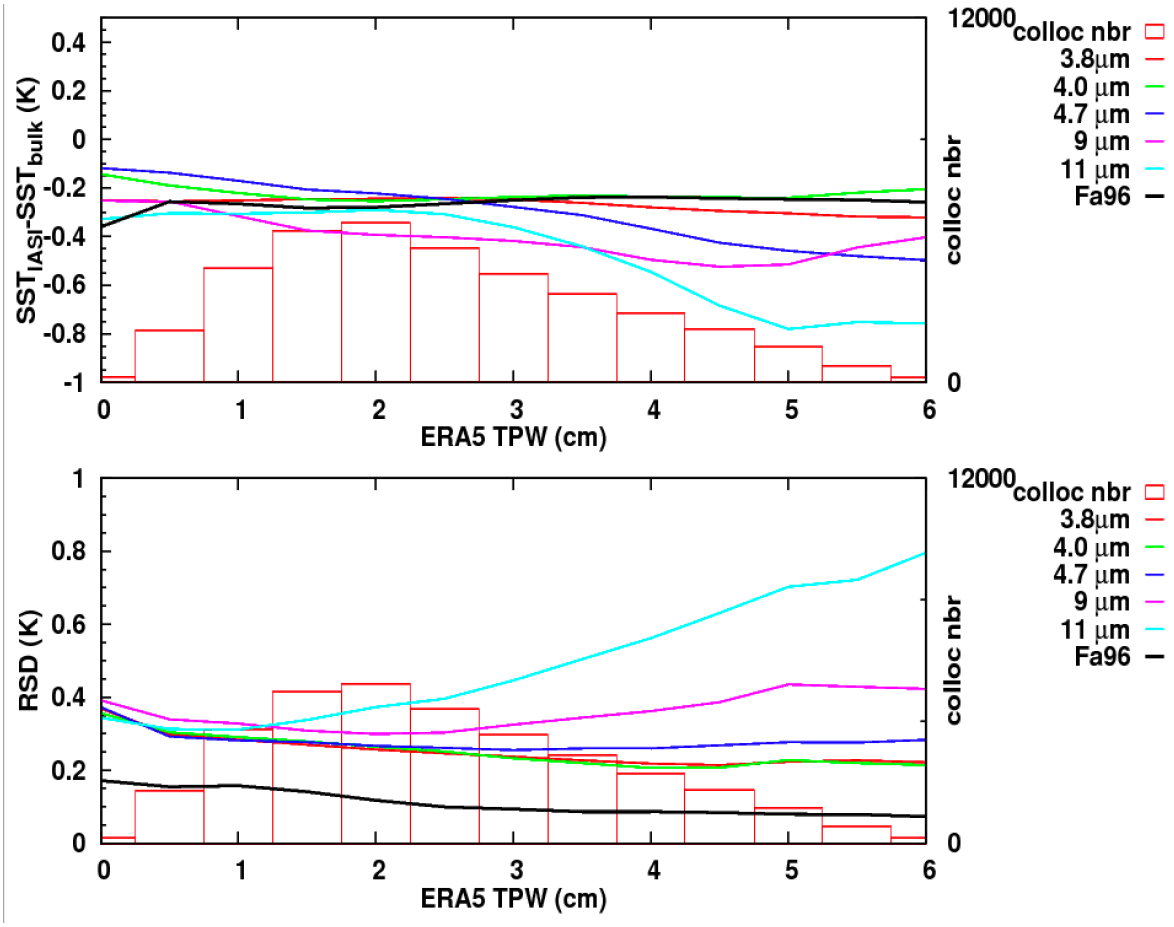

Figure 2: ΔT=T_{Skin}-T_{Bulk} values (median and robust standard deviation) obtained from SSTs retrieved from the five different regions (color lines) of the IASI spectra as functions of the ECMWF ERA5 total precipitable water (TPW) content of the observed atmospheres. The black line corresponds to the ΔTs computed using the model of Fa96 with ERA5 heat exchange data. All values have been averaged over a sweeping TPW bin of 1 cm. The red boxes and right hand side y axis scale indicate the number of data points (i.e. of collocations used).

Figure 2 displays the median and the RSD obtained for the difference ΔT between the IASI SST and in-situ measurements versus the total precipitable water taken from ERA5. The results based on the use of the 3.8 µm, 4.0 µm, 4.7 µm, 9.0 µm and 11 µm spectral regions are displayed together with the predictions made using Fa96. As can be seen, the median and the RSD are relatively insensitive to the TPW for the SSTs retrieved at 3.8 µm: ΔT =-0.26 K for TPW<4 cm, and the absolute value increases slightly for more humid atmospheres (ΔT =-0.32 K for TPW=6 cm). The results obtained from the 4 µm region are very similar, but ΔT here remains more constant throughout the entire TPW range. The RSDs for these two wavelength ranges are very close to each other, with an almost TPW-independent value lower than 0.25 K, except for a slight increase below 1.5 cm TPW. The ΔTs retrieved at 3.8 and 4.0 µm are both consistent with those predicted following Fa96, which show a weak influence of the TPW with an almost constant ΔT value around -0.25 K and a small amplitude (+/-0.03 K) of variation. The RSD for Fa96 is lower by a factor of about two, but it results only from the geophysical variability of the cool-skin effect, without any contribution from errors coming from the observation or parametrization. For the SSTs retrieved at 4.7 µm, the medians and RSDs are consistent with those obtained at shorter wavelengths for TPWs between roughly 1 and 3 cm. For large TPW contents, the RSD is slightly larger which, given the higher sensitivity of this spectral region to atmospheric humidity (see Appendix A1), can be explained by the random errors made on the input water vapor profile. Meanwhile, ΔT becomes more and more negative as the TPW increases above 3 cm. As discussed below for the long wavelengths, this can be due to

systematic errors in the radiative transfer due, for instance, to the water vapor continuum parametrization or/and to a systematic underestimation of the water profile. For the SSTs retrieved at 9 and 11 µm, the RSDs get larger as the TPW increases, as expected given their significant sensitivity to the water profile (Appendix A1). As for the restitution at 4.7 µm, the ΔTs obtained at 11µm and, to a lesser extent, at 9 µm, tend to become more negative when the TPW increases, suggesting a systematic error on the water vapor continuum. Indeed, a sensitivity analysis (see Appendix A2), shows that an increase of 5% of the H_2O self continuum, largely compatible with the uncertainties in this spectral region (Mlawer, 2020), could explain this behavior. A quite systematic cold bias of about -0.1 K is additionally observed for the SSTs retrieved at 11 µm (with respect to the previously discussed values), even for very dry atmospheres. This may be explained by systematic errors in the radiative transfer calculations inputs as, for example, on the surface emissivity, since changing the latter by only +0.003 (consistent with the uncertainty, see e.g. Newman et al., 2005) here modifies the retrieved SST by -0.1 K (see also Appendix A1).

The results discussed above are consistent with previous studies highlighting the difficulty of using the 8-12 µm spectral range to retrieve SSTs, due to high sensitivities to the water vapor and temperature profiles (Embury et al., 2012; O'Carroll et al., 2012; Kilpatrick et al., 2015), as well as to the surface emissivity which depends on the salinity and the SST itself (Pinkley et al., 1977; Newman et al., 2005). The SSTs retrieved at 4.7 µm also present sensitivities to the profiles, but which are more limited. Finally, the SSTs retrieved at 4.0 and 3.8 µm, which are the least sensitive to the atmospheric humidity, are highly consistent with each other. A slight difference is observed for very humid atmospheres, but without any increase of the RSD for both restitutions, preventing to conclude on which spectral region provides the most accurate results. Hence, from now on, only the SSTs retrieved at 3.8 µm are discussed given their better stability and the fact that the atmospheric transmission is the highest in this wavelength region (see Fig. 1).

Together with the results obtained using IASI data around 3.8 µm, Fig. 3 displays the ΔT variations with the TPW derived from several other SST products collocated with IASI: The ECMWF ERA5 skin SSTs, EUMETSAT IASI-L2 SSTs (O'Carroll et al., 2012, see also the technical document EUM/TSS/REP/13/684650 on the website https://www.eumetsat.int/website/home/Data/TechnicalDocuments/index.html), the L3C CCI AVHRR/Metop-A v2.0 products (Merchant et al., 2014) available at https://cds.climate.copernicus.eu/, and two MODIS-Terra SST 9 km-mapped products (Kilpatrick et al., 2015) available at http://oceandata.sci.gsfc.nasa.gov: The first (referred to as the NSST) is derived from MODIS bands 31 and 32 (λ = 11 and 12 µm, respectively), while the second (SST4) is retrieved from measurements in the 4 µm atmospheric window (bands 22 and 23). It should be emphasized that the MODIS products are based on empirically-derived coefficients obtained from a match-up database of in-situ bulk temperature measurements and converted to skin temperature by subtracting 0.17 K, in order to take the cool-skin effect and associated T_{Skin}-T_{Bulk} difference through the averaged value of (Donlon et al., 2002). MODIS products are therefore *not* independent from in-situ measured data. For all other satellite SST products, only their highest quality data are retained, namely: quality flag 5 for AVHRR/Metop-A data, for the IASI-L2 SSTs only the pixels flagged clear and for which the iteration procedure converged, and only quality level "0" data from MODIS. Note that the same in-situ buoy measurements datasets collocated with IASI have been used for comparisons with the other SST products. This introduces a systematic time shift for the observations by MODIS which crosses the equator at 22:30. Recall that the set of collocated in-situ measurements that we selected (Sec. 3.1.3) depends on the cloudy-scene filtering (Sec. 2.4) used. Consequently, the number of observations finally retained slightly differs from one product to another, due to

differences in the quality flags (and in particular in cloud filtering). About 58% of the 16411 selected collocations are kept for EUMETSAT IASI-L2, 49% for MODIS-NSST and for MODIS-NSST4, 76% for AVHRR, and 99.7% for ERA5.

Figure 3 shows different behaviors for the various SST products. First, all ΔTs are not centered on the same value. Those from IASI_3.8 are, as discussed above, consistent with FA96, around -0.25 K, and those from ERA5 have an offset of about -0.05 K when compared to IASI_3.8. The MODIS SST4 and NSST ΔTs are centered around -0.17 K in the medium range of TPWs, as expected considering the method of retrieval (Kilpatrick et al., 2015) recalled above (i.e, the MODIS SST is a "bulk" temperature corrected by -0.17 K). They have an offset of about +0.1 K when compared to IASI_3.8. Finally, the ΔTs from AVHRR are centered around -0.1 K (with +0.15 K with respect to IASI_3.8), and those from IASI-L2 are around 0.K (+0.25 K when compared to IASI_3.8), implying SSTs calibrated as bulk rather than skin temperatures. The dependence on the atmospheric humidity highly varies with the considered product. When disregarding their respective offsets, the IASI_3.8, ERA5 and AVHRR ΔTs behave similarly with the TPW, with stable ΔTs for TPW<4 cm, and a slight decrease of the value for higher TPWs. The MODIS SST4 ΔT behaves similarly, but the decrease is larger for TPW>4 cm, and the MODIS NSST ΔT is the most variable with a nearly constant decrease from 0 K to -0.5 K. This behavior is consistent with Kilpatrick et al. (2015), who concluded that MODIS SST4 is superior to NSST thanks to the fact that the atmosphere is more transparent in the spectral region used. Finally, the ΔT for IASI-L2 is practically constant in the 1.5-4.0 cm TPW range, but takes positive values (reaching +0.25 K for a TPW of 6 cm) for both very dry and wet atmospheres. The RSDs, which result from errors in both the SST products and in-situ measurements (~0.21K) as well as from natural variations for a given range of TPW, are similar for IASI_3.8 and AVHRR, with behaviors close to that of the FA96 RSD (with an offset of 0.15 K). The RSDs for MODIS SST4, IASI-L2 and ERA5 are a little larger, those of MODIS SST4 and IASI-L2 increasing slightly with the TPW, implying a decrease of the precision with increasing humidity. The RSDs for MODIS-NSST are the largest, with a strong increase with the TPW, as previously shown (Kilpatrick et al., 2015).

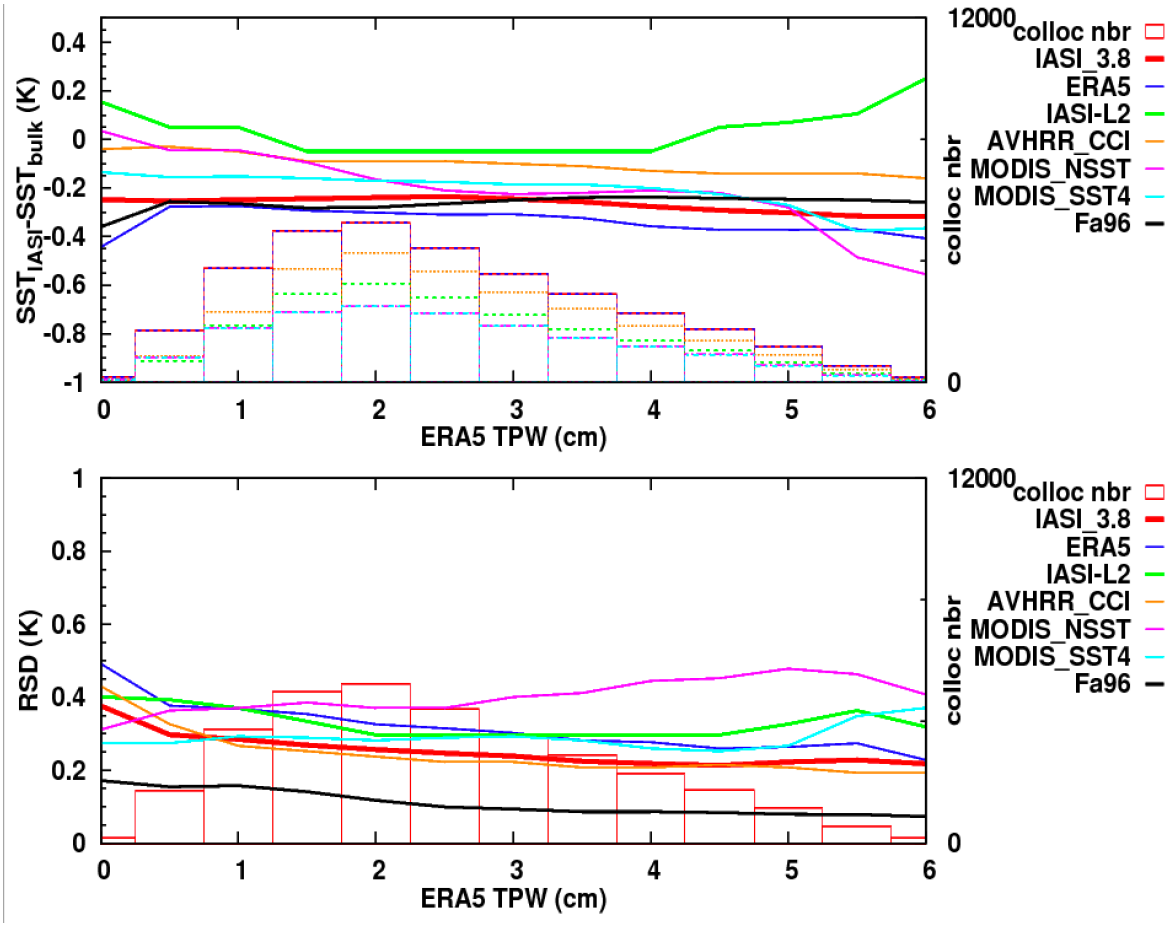

Figure 3: Same Figure 2, but here for comparisons between different SST products: SST IASI at 3.8 µm (this work), ECMWF ERA5, EUMETSAT IASI-L2, AVHRR_CCI, and two MODIS-Terra SSTs 9km-mapped products: NSST and SST4, retrieved from long- and short-wave channels, respectively. For these comparisons, the collocations used, with numbers indicated by the colored boxes and right hand side y axis scale (for all SST products in the top plot and only for IASI_3.8 in the bottom one), come only from Metop-A and for the year 2016.

3.3.2 Influence of the wind speed

Figure 4 presents the variations of ΔT with the wind speed provided by ERA5 for the same SST products as in Figure 3, together with the predictions made following Fa96. As demonstrated in several previous studies (e.g. Fairall et al., 1996; Donlon et al., 2002; Zhang et al., 2020), the wind speed has a significant influence on ΔT. Fast winds lead to a strong turbulent mixing that reduces $|\Delta T|$, whereas for slow winds the difference between T_{Skin} and T_{Bulk} is larger. Here, the IASI_3.8 ΔT is very consistent with Fa96 for wind speeds lower than 10 m.s^{-1}, with differences below 0.05 K. For wind speed above 10 m.s^{-1}, the ΔTs from IASI_3.8 become more different from the FA96 predictions, with an offset of about -0.1 K for a speed of 15 m.s^{-1}, while the RSD remains the same, showing a stable error against wind speed. Below 10 m.s^{-1}, the relative variations of the IASI_3.8 ΔT are consistent with the other satellites products, when disregarding their respective offsets which are consistent with the results in Figure 3 (i.e: +0.25 K for IASI-L2, +0.15 K for AVHRR and +0.1 K for the two MODIS). Above 10 m.s^{-1}, the differences are slightly more important.

The IASI_3.8 ΔT, which is ≈-0.4 K for slow winds, tends toward a constant value around -0.22 K for wind speeds above 8 m.s^{-1}. From this point of view, the ΔT from ERA5 behaves differently than the others, with a stronger cold skin effect for low wind speeds, and a value consistent with FA96 for strong winds. The RSDs are similar to those displayed in Figure 3,

with lower values for IASI_3.8 and AVHRR, consistent values for ERA5, IASI_L2 and MODIS SST4 and the highest value for MODIS NSST.

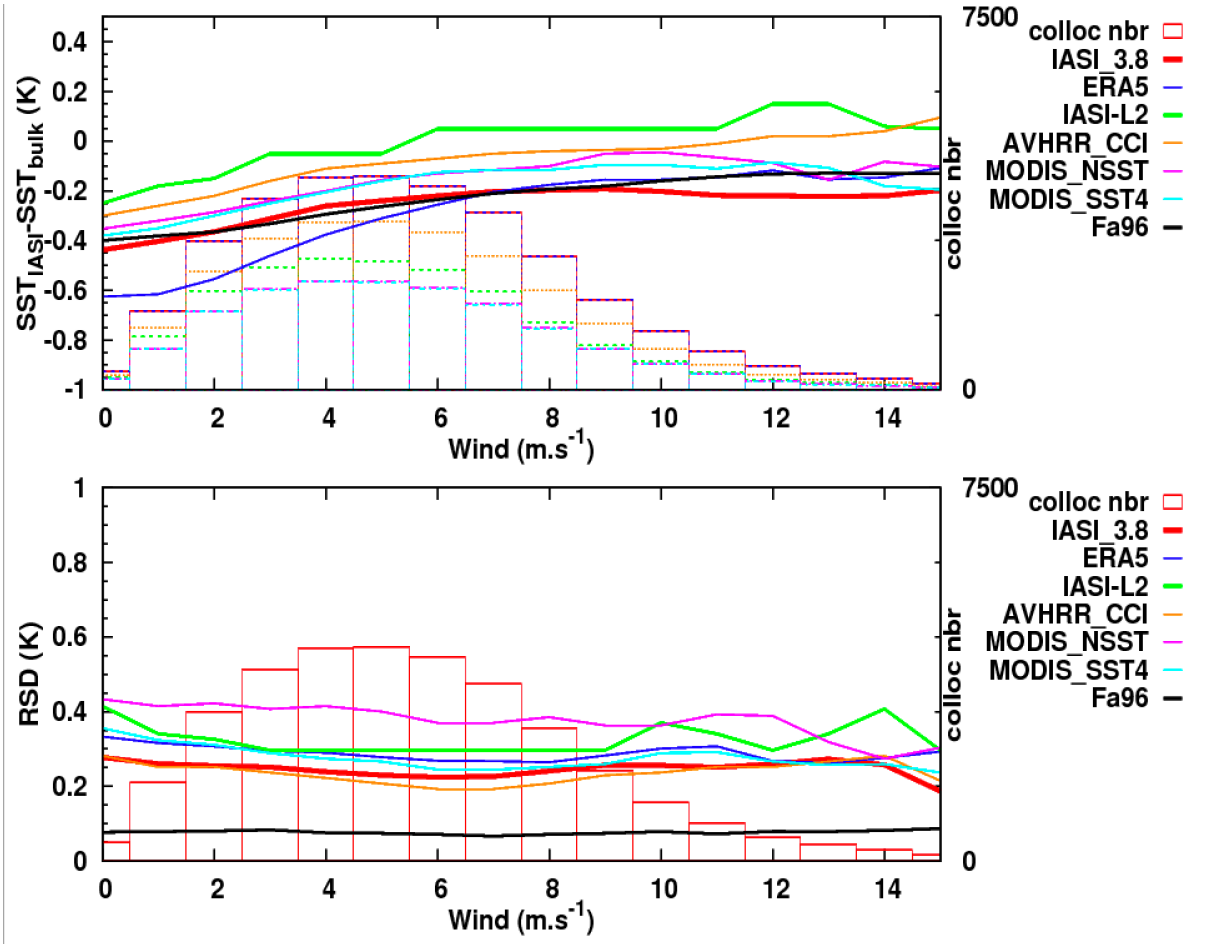

Figure 4 : Same as Figure 3, but as functions of the ERA5 wind speed. Averages are calculated over bins of 1 m.s^{-1}.

The Fa96 (Fairall et al., 1996) model of the cool-skin effect, as others proposed in (Saunders, 1967; Liu et al., 1979; Soloviev and Schlüssel, 1994; Castro et al., 2003; Zhang and Zhang, 2012), is interesting because it relates ΔT to some characteristics of the considered sea-spot +atmosphere and is thus physically-based. However, its use is not straightforward because various local quantities (radiative flux, sensible and latent heat exchanges, friction velocity) must be known. This is why much more simple models have been proposed in which ΔT is parameterized as a function of the wind speed only (Donlon et al., 2002; Horrocks et al., 2003; Minnett et al., 2011; Alappattu et al., 2017; Zhang et al., 2020). These approaches write:

$$\Delta T = a + b \exp\left(-\frac{U}{U_0}\right) \quad (3)$$

in which U is the wind speed (at 10 m) and the empirical parameters a, b, and U_0 are determined from simultaneous measurements of both T_{Skin} and T_{Bulk}. The results retrieved from IASI in the 3.8 µm region are compared with the available empirical models in Figure 5, calling for the following remarks. The first is that there is a dispersion between the various models, with large differences for slow winds between (Minnett et al., 2011) and (Alappattu et al., 2017) and the other datasets. Except for these two models, all others agree, throughout the investigated wind speed interval, within about +/- 0.05 K, a dispersion largely within uncertainties. For strong winds, all models predict a plateau but at a level that varies by about +0.3 K from the minimum (Alappattu et al., 2017) to the maximum value (Horrocks et al., 2003). The second remark is

that the values retrieved in the present study from IASI spectra agree very well with the (most recent) model of (Zhang et al., 2020) up a wind speed of about 9 m.s^{-1}. Above this limit differences increase and reach about 0.04 K, a value that likely largely remains within the uncertainty of the measurement and model. Finally note that a fit of the IASI_3.8 results using Eq. (3) over the U=0-15 m.s^{-1} range of Figure 5 leads to a=-0.20 K, b=-0.26 K and U_0=3.08 m.s^{-1} (see Figure 5). Limiting the fitting range to the U=0-9 m.s^{-1} interval yields a=-0.12 K, b=-0.33 K and U_0=5.18 m.s^{-1}, values that agree well with those (a=-0.15 K, b=-0.33 K and U_0=4.35 m.s^{-1}) given in (Zhang et al., 2020).

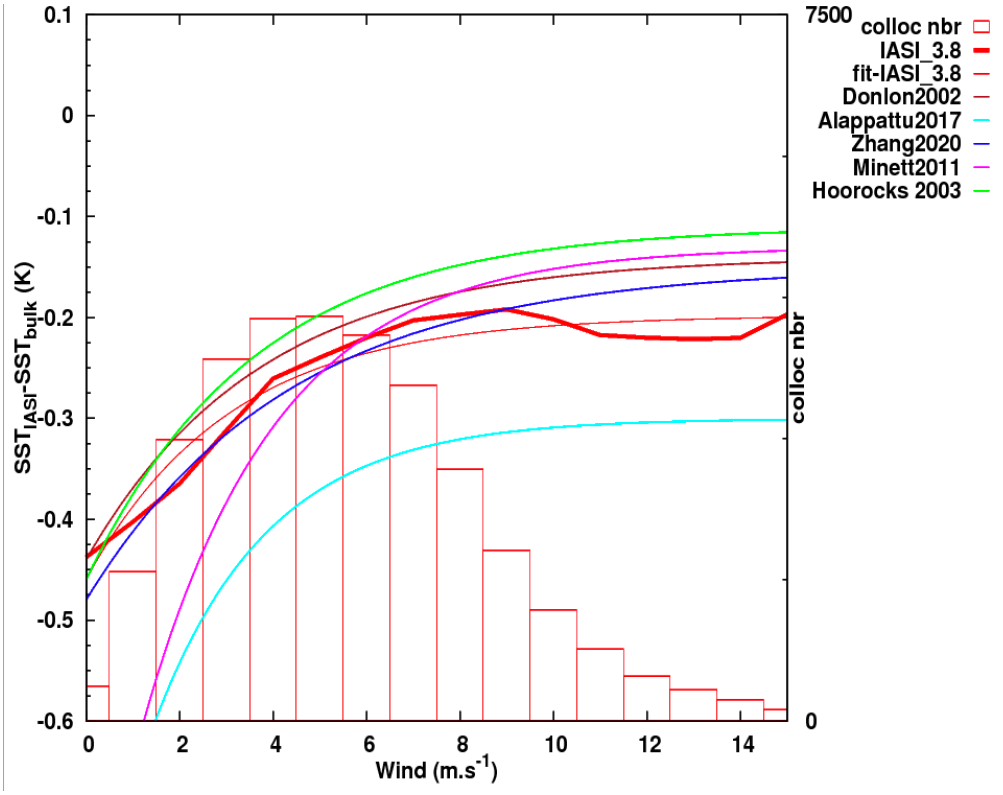

Figure 5: Influence of the wind speed (from ERA5) on the ΔT=T_{Skin}-T_{Bulk} values (median) obtained from SSTs retrieved from the 3.8 µm region of the IASI spectra (IASI_3.8) and comparison with the empirical models [Eq. (3)] of (Donlon et al., 2002; Horrocks et al., 2003; Minnett et al., 2011; Alappattu et al., 2017; Zhang et al., 2020). fit-IASI_3.8 denotes the fit of the IASI_3.8 results using Eq. (3). The red boxes and right hand side y axis scale indicate the number of data points (i.e. of collocations used).

3.3.3 Influence of the air-sea temperature difference

Figure 6 displays the dependences of the various ΔTs on the difference, provided by ERA5, between the air temperature at 2 meters above the surface and the in-situ measured bulk temperature (T_{2m}-T_{Bulk}) for the same SST products as in Figure 3 and Figure 4. As previously observed [see (Zhang et al., 2019) and references therein], (T_{2m}-T_{Bulk}) has a significant influence on ΔT. Situations where the air is significantly colder than the sea enhance the (positive) heat transfers from the ocean to the atmosphere, increasing the cool skin effect. Consistently, as (T_{2m}-T_{Bulk}) increases, and eventually becomes >0, the surface-to-atmosphere fluxes reduce with, in particular, of change of sign of the sensible heat exchanges, and ΔT is then expected to get closer to 0 K and it may even to change sign. The results obtained from IASI spectra near 3.8 µm are globally consistent with these simple physical considerations. For moderate air-sea temperature differences, between -4 K and +4 K, the number of collocations is maximum and the IASI_3.8 ΔT values closely follow Fa96, as observed before. Here again, the other satellites products almost show the same behavior as IASI_3.8, but with the biases

pointed out in the previous figures. MODIS NSST is however slightly more "noisy" and the IASI_L2 ΔT increases more rapidly with T_{2m}-T_{Bulk}, a behavior further amplified in the case of the ERA5 product. For (T_{2m}-T_{Bulk})>2.5 K, ΔT becomes positive for ERA5 and IASI-L2, contrary to the other products for which ΔT approaches 0 K but remains negative. A continuous positive increase of ΔT with increasing (T_{2m}-T_{Bulk}) was also observed with AATSR SST data as shown in Fig. 4 of (Zhang et al., 2019), but with a larger amplitude of variation of ΔT, from about -0.25 K for (T_{2m}-T_{Bulk}) ≈-5 K to +0.5 K for (T_{2m}-T_{Bulk}) ≈4 K.

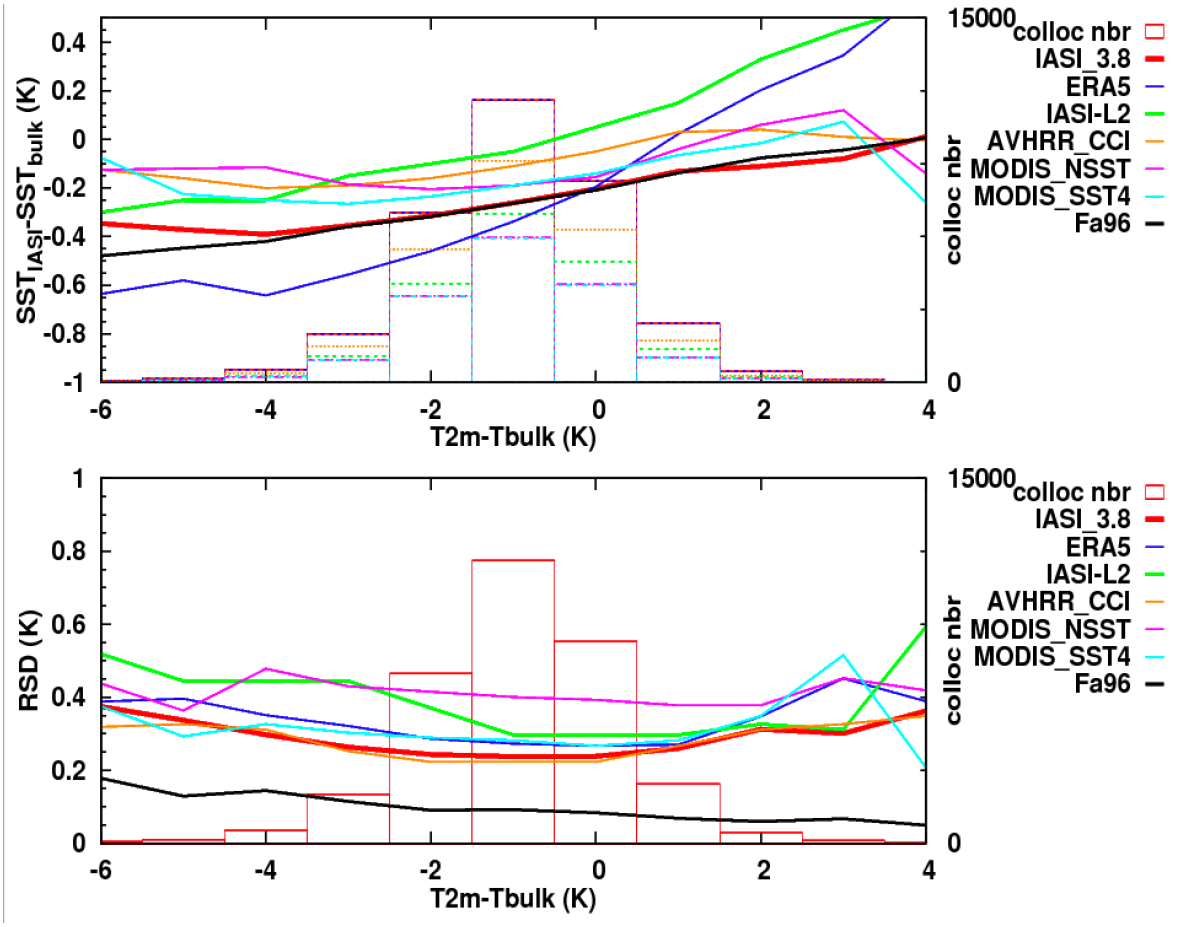

Figure 6 : Same as Figs. Figure 3 and Figure 4, but here as functions of the air-sea temperature difference (T2m-Tbulk) provided by ERA5, averaged over a bin of 1 K.

3.3.4 Summary

Sections 3.3.1-3.3.3 demonstrate that our retrieved values closely follow the predictions made using (Fairall et al., 1996), as well as the empirical relationship of (Zhang et al., 2020) for wind speed, implying a good accuracy, with a very small bias. Indeed, the observed variations of our results agree with what is theoretically expected, i.e.: a strong sensitivity to wind speed, with a larger cold skin effect for low wind speed and a stabilization for strong winds, a quasi linear relationship between ΔT and T_{2m}-T_{Bulk}, and, finally, a weak effect of the TPW, implying a correct accuracy even for very humid situations. The RSD is in general stable for any variation of the observed scene parameters and close to the in-situ measurement error [0.21 K, (Xu and Ignatov, 2016)], which demonstrates that a good precision is achieved. In contrast, the other products (satellites and models), which are more or less independent of the buoys measurements as discussed above, show a large spread of biases with respect to IASI_3.8 and FA96.

4 Toward a long IASI time series

Assessments of the quality of the IASI retrieved SSTs have been presented and discussed in Sec. 3 through comparisons with in-situ measurements, using Metop-A data for the year 2016, showing a close match with the theoretical FA96 skin to bulk temperature differences. Here, we now analyze the stability of the retrievals with time over the whole Metop-A period, as well as the consistency between Metop-A, -B, and -C, which is mandatory to build-up reliable long-time series. For this, the IASI and in-situ temperatures are compared in term of a difference in bulk temperature ΔT_{Bulk}=T_{Bulk}(IASI_3.8)-T_{Bulk}(in situ), where T_{Bulk}(IASI_3.8) has been obtained by subtracting, from the SST T_{Skin} retrieved from IASI at 3.8 µm, the theoretical ΔT= T_{Skin} -T_{Bulk} calculated from FA96 using the ECMWF flux estimates. It should be noted that this conversion may introduce some errors, but it is convenient since it enables easier to analyze comparisons by removing a large part of the variation of ΔT due to the conditions of observations (wind speed, TPW, air-sea temperature difference, seasonal effect, etc…).

4.1 Time series of ΔT_{Bulk} from Metop-A and Metop-B

Figure 7 presents, for all the collocations, the time series of the monthly median ΔT_{Bulk} observed between the converted IASI bulk temperatures and the collocated *i*Quam in-situ measurements for Metop-A (since January 2008) and Metop-B (since February 2013). The lower part of each panel displays the differences between the values obtained from Metop-B (ΔT_B) and Metop-A (ΔT_A). The results are shown separately for four regions: worldwide, the equatorial (from -20°S to 20°N), northern (20°N to 50°N) and southern (-50°S to -20°S) mid-latitudes.

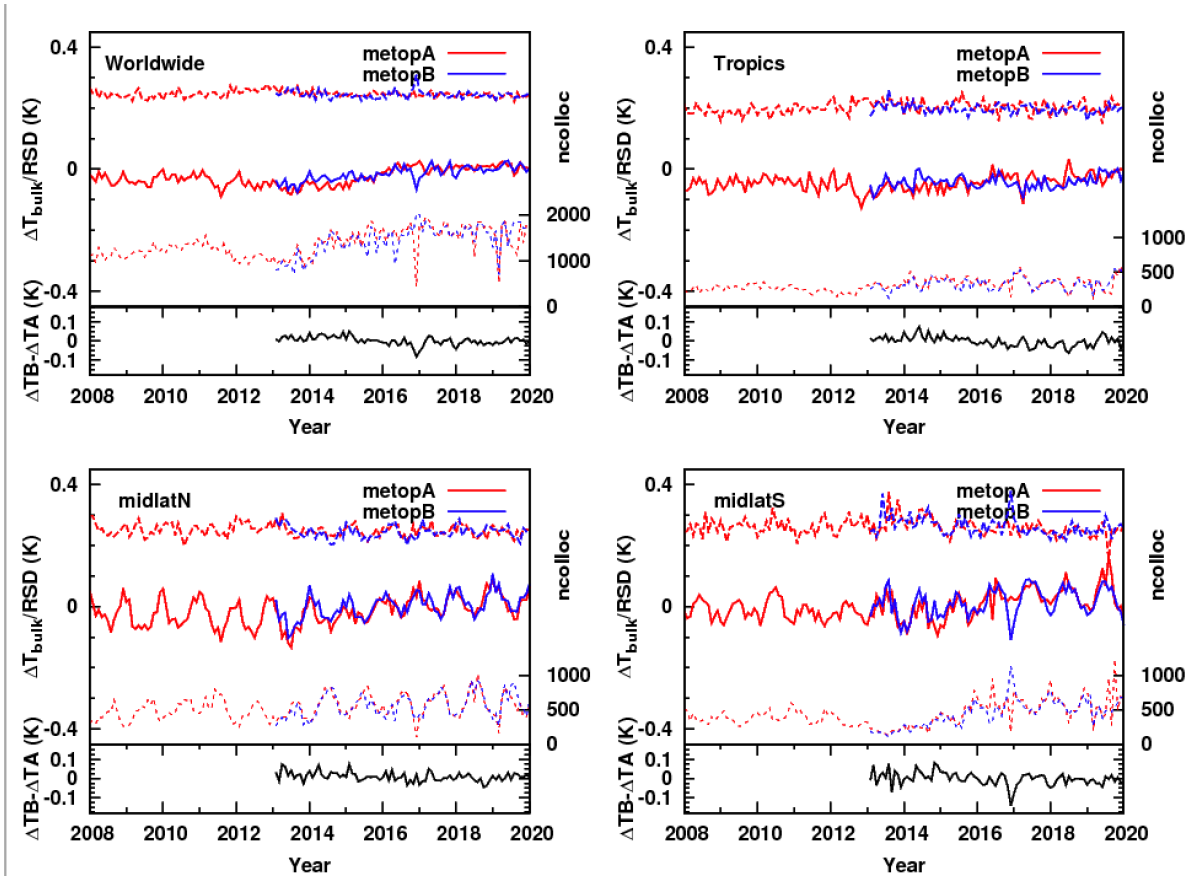

Figure 7 : Time series of the monthly ΔT_{Bulk} observed between the converted IASI bulk temperature and *i*Quam for Metop-A (red) and Metop-B (blue) for different regions. Solid lines correspond to the median, dashed lines to the associated RSD, and dotted line to the number of collocations (read on the right y axis). Top left: worldwide; top right: tropics; bottom left: Northern mid-latitudes; bottom right: Southern mid-latitudes. At the bottom of each

graph, le black line represents the (double) difference between Metop-B ΔT_{Bulk} (ΔT_B) and Metop-A ΔT_{Bulk} (ΔT_A). The corresponding IASI-retrieved bulk temperatures have been obtained by subtracting the $\Delta T = T_{Skin} - T_{Bulk}$ estimated from FA96 from the skin temperature T_{Skin} retrieved from the 3.8 µm region in the IASI spectra.

Table 2 summarizes the corresponding statistics with the values of the median of ΔT_{Bulk} and of the RSD averaged over the 2008-2020 time period. For both quantities, the slope of their linear trend with time as well as the 95% confidence interval are also given, which are in bold characters when significant (i.e. when the absolute value of the trend is larger than the 95% confidence interval). The double difference $\Delta T_B - \Delta T_A$ is given in the last line of the table.

Table 2 : Statistics of the IASI- *i*Quam comparisons for the whole available period (i.e 2008-2019 for Metop-A and 2013-2019 for Metop-B) and for the 4 geographical regions used in Figure 7.

IASI_bulk- *i*Quam		World wide	-20° to +20°	20° to +50°	-50° to -20°
Median ΔT_{Bulk} (K)	Metop-A	-0.025+/- 0.028	-0.045+/- 0.026	-0.017+/- 0.045	-0.002+/- 0.043
	Metop-B	-0.015+/- 0.023	-0.042+/- 0.021	0.002+/- 0.004	0.014+/- 0.045
Trend of the median ΔT_{Bulk} in mK/yr (95% interval)	Metop-A	**4.5 (1.1)**	**2.4 (1.2)**	**4.6 (2.0)**	**5.5 (1.8)**
	Metop-B	**8.7 (1.7)**	**2.6 (2.3)**	**9.6 (2.0)**	**7.1 (4.8)**
RSD (K)	Metop-A	0.246+/-0.011	0.201+/-0.020	0.251+/- 0.022	0.261+/- 0.025
	Metop-B	0.244+/-0.013	0.199+/-0.015	0.244+/- 0.019	0.263+/- 0.030
Trend of the RSD/ in mK/yr (95% interval)	Metop-A	-0.4 (13.0)	1.0 (11.8)	-0.9 (12.8)	-1.0 (12.5)
	Metop-B	-0.9 (29.3)	-1.9 (27.2)	0.1 (27.3)	-5.7 (28.2)
(Metop-B)-(Metop-A) $\Delta T_B - \Delta T_A$ difference (K)		0.002+/-0.022	-0.002+/- 0.026	0.010+/- 0.024	-0.000+/- 0.034

The overall bias $|\Delta T_{Bulk}|$ is lower than 0.05 K in all regions and practically constant over the whole period, with an averaged value of -0.025 K (+/-0.028 K) for Metop-A and -0.015 K (+/- 0.023 K) for Metop-B. Note that these values are consistent with the systematic underestimation of the amplitude of the cool-skin effect in FA96 pointed out in (Zhang et al., 2020). The largest absolute bias is obtained in the Tropics (-0.045 K) and the largest variations around the mean are observed in the northern mid-latitudes (and to a lesser extent in the southern) where a seasonal cycle is clearly observed (see Figure 7). Note that the amplitude of this variation is slightly lower when direct comparisons between IASI skin temperatures and bulk temperature measurements are made (not shown), consistent with former observations that the skin effect correction does not decrease the standard deviation (e.g. Embury et al., 2012) while having a positive impact on the bias. Keeping in mind the uncertainties due to the skin-to-bulk conversion, coming from the estimated ERA5 fluxes and the FA96 parametrization, this demonstrates the accuracy of the retrieved IASI SSTs, which have a precision better than the required accuracy of 0.1 K needed for climate datasets (Ohring et al., 2005). In addition to this successful achievement, a second important result obtained here is the very good agreement between the values retrieved from Metop-A and Metop-B. Indeed, the differences $\Delta T_B - \Delta T_A$ in

Figure 7 and Table 2 demonstrate the strong consistency from one platform to the other, with a mean difference < 0.01 K associated with a standard deviation < 0.04 K. This successfully opens, as confirmed below, the possibility to have access to a homogeneous long time series combining the three successive IASI, which is a prerequisite for climate studies.

The temporal stability over the whole record is assessed through the analysis, with a linear time trend model, of the series of the IASI-*i*Quam bulk temperature differences. In some studies, in order to attenuate the impact of seasonal biases that may appear as auto-correlated error and affect the trend estimation, the time series is pre-whitened using, for example, a lag 1 auto-regressive (AR1) model (e.g. Merchant et al., 2012; Berry et al., 2018). But since this may attenuate a real trend if there is one (see e.g. Hamed, 2009 and references therein), we here assume that there are no auto-correlations between months and do not apply any pre-treatment. Table 2 shows that the worldwide trend for Metop-A is +0.045 K/decade, with a 95% confidence interval of 0.01 K/decade. This value is slightly greater than the required stability of 0.04 K/decade recommended for climate studies in (Ohring et al., 2005). However, in the 20°S-20°N tropical band, the obtained trend of 0.024 K/decade fully satisfies this requirement. This result assesses the radiometric stability of IASI, even if, considering the 95% confidence interval of 0.012 K/decade, this value is significant. Concerning collocations outside the tropics, the trend in the Northern regions is similar to the global one, while a larger value (0.055 K/decade) is obtained in the South. It should be emphasized that this positive trend is connected with a change in the mean ΔT_{Bulk} after 2015, and also associated with an increase of the number of collocations (in particular in the southern hemisphere). We cannot exclude the possibility that the latter may contribute to the observed shift in the time series through a change in the geographical distribution of the collocations. Trends observed for Metop-B are larger in the extra-tropics (with values between 0.07 and 0.1 K/decade), but the period of time considered is too short when compared to the inter-annual variations of ΔT_{Bulk} for this result to be fully significant. Within the 20°S-20°N band however, the trend is, as for Metop-A, lower than the required value of 0.04 K/decade (0.026 K/decade with a 95% confidence interval of 0.023 K/decade).

The analysis of the variation with time of the standard deviation of the IASI-*i*Quam bulk temperature differences is important to assess the precision of the data record. Here the standard deviation is almost constant over years, with a mean value around 0.25 K and a standard deviation between 0.01 and 0.03 K depending on the region considered. Note here again the extreme consistency between Metop-A and Metop-B, even if the associated periods of time are not the same. For both instruments, there is no time evolution of the standard deviation (see Figure 7), confirming the high stability of the precision over years and the excellent continuity between the two instruments.

4.2 Direct comparisons between Metop-A, Metop-B and Metop-C

The main aim of this section is to assess the consistency of the SSTs retrieved from the entire Metop suite, which would enable to provide long time series of at least 20 years from Metop-A to Metop-C. When considering the data obtained from different instruments, it may be difficult to obtain consistency between them and some discontinuity may appear at each change of instrument. The main advantage of the IASI suite is, from this point of view, that the radiometric consistency of the three instruments was ensured during the building of the sensor (Hewison et al., 2013; EUMETSAT, 2014). A first successful check of this consistency was brought by Figure 7 through comparisons of the differences between the temperatures obtained for Metop-A and Metop-B with in-situ measurements. In order to go further, we below directly compare the monthly averages of the retrieved skin temperature over 1°x1° grids, obtained separately from each instrument. Note that, since the two satellites are localized in opposition on the same orbit, they do not observe the same location on the same day. This is why the

comparisons are made below on a monthly instead of a daily scale. For each month and each 1° grid cell the (Metop-B)-(Metop-A) SSTs difference is considered only if the monthly mean is calculated from more that 5 observations for each instrument and if the resulting standard deviation is smaller than 1.2 K. Table 3 gives the results for (Metop-B)-(Metop-A) for the 2013-2020 period, i.e. the averaged of each monthly grid cell differences from February 2013 to January 2020. Similarly, the (Metop-C)-(Metop-A) and (Metop-C)-(Metop-B) statistics are also given from July 2019 to June 2020. The (Metop-B)-(Metop-A) bias is small (-0.005 K) and close to the median (-0.004 K), indicating that the differences are almost normally distributed, without any unbalance from one instrument to the other. The RSD is small (0.25 K) and lower than the standard deviation (0.33 K), a difference due to lower statistics and/or indicating the presence of some outliers in the comparisons, probably due to the presence of undetected clouds. This is confirmed by Figure 8, where the bias is noisier and the standard deviation is larger in regions where the presence of clouds is frequent, particularly in the high latitudes. In contrast, in the tropics where clouds are rarer, the standard deviation is generally below 0.2 K. This demonstrates the low dispersion between Metop-A and Metop-B, especially since a significant part of the standard deviation comes from the natural day-to-day variations of the SST within a month, given that Metop-A and Metop-B do not observe the same grid-cell on the same day. It should finally be emphasized that the difference between the data provided by Meteop-A and Meteop-B (see Figure 8) is almost constant over the globe, with no clear geographical dependence that could be linked to humidity or temperature variations.

Table 3: Global mean difference between the monthly nighttime 1°x1° SST of Metop-B - Metop-A over the 2013-2020 period, Metop C – Metop B and Metop C – Metop A over the 2019-2020 period (statistics and robust statistics).

(Metop-B)-(Metop-A) (2013-2020)		(Metop-B)-(Metop-A) (2019-2020)		(Metop-C)-(Metop-A) (2019-2020)		(Metop-C)-(Metop-B) (2019-2020)	
Bias/ SD (K)	Median/ RSD (K)	Bias/ SD (K)	Median/ RSD (K)	Bias/ SD (K)	Median/ RSD (K)	Bias/ SD (K)	Median/ RSD (K)
-0.005/ 0.333	-0.004/ 0.251	-0.016/ 0.312	-0.015/ 0.234	-0.032/ 0.227	-0.031/ 0.162	-0.016/ 0.307	-0.016/ 0.230

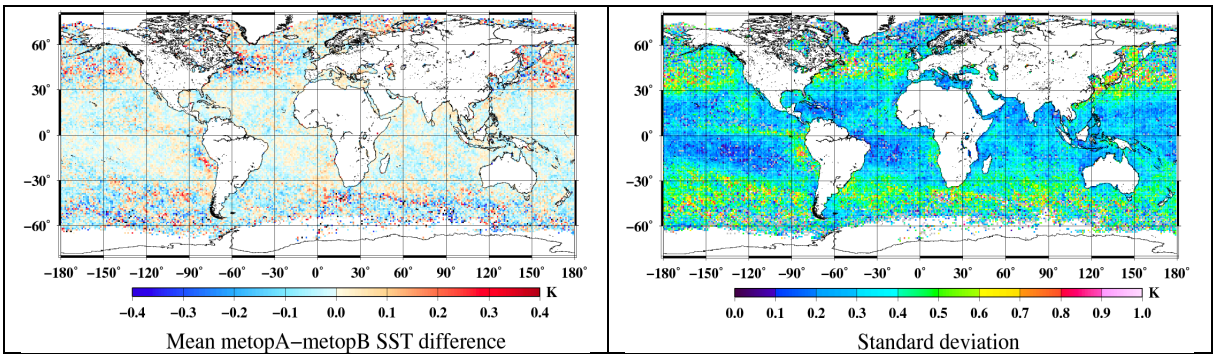

Figure 8 : Left: Mean difference between the monthly nighttime 1°x1° SST retrieved from Metop-A and Metop-B IASI spectra (Metop-B – Metop-A) over the 2013-2020 period. Right: Associated standard deviation.

The preceding results show that the restitutions from Metop-A and Metop-B can therefore be considered as fully consistent. Similar results are obtained over the 2019-2020 period with Metop-C when compared to both Metop-A and Metop-B. This implies that: (1) The Metop-A time series can be extended by Metop-B or/and -C observations while keeping a homogeneous dataset. (2) During the overlap period of two (or three) instruments, the revisit time delay can

be significantly decreased by the simultaneous use of the two (or three) flying instruments, providing a daily complete coverage of the globe (except over clouds) that cannot be achieved by using of a single instrument. This is exemplified by Figure 9, for 19th August 2016, demonstrating the significant increase of the spatial coverage brought by the use of both Metop-A and –B. Note that this coverage could be further increased by using all recordings within the +/-50° θ swath and no more disregarding, as done in this study, the spectra collected for |θ|>30°. Let us however recall that this would then require to take the influence of wind speed on the sea surface emissivity ε_s (Masuda et al., 1988). Indeed, the latter cannot be neglected for large viewing angles without large consequences (see the sensitivity to ε_s in Appendix A1) on the retrieved SST.

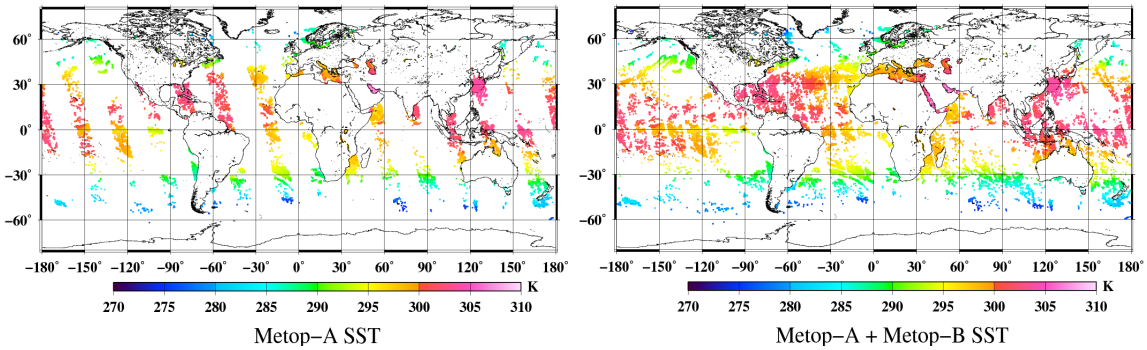

Figure 9 : Left : Skin SST retrieved from IASI/Metop-A spectra recoded on 19th August 2016. Right: Skin SST retrieved by both IASI/Metop-A and IASI/Metop-B spectra recorded the same day.

4.3 Global SST anomaly time series and comparisons with other products

The detailed analysis of the evolution over time of the IASI-retrieved skin SST from a climate-evolution point of view is far beyond the scope of this paper. However, as a final validation and since it opens promising perspectives, we now present the global skin-SST anomaly time series within the 2008-2020 IASI period and compare it with results obtained from other SST products. To compute the de-seasonalized monthly anomalies, a monthly climatology is first calculated, defined as the monthly-averaged SST over the 13 years for every 1°x1° grid point. The monthly anomaly time series is then built by calculating every difference between the monthly SST and the monthly climatology for each grid cell, each month and each year. The region studied is restricted to 60°S-60°N, in order to avoid potential biases due to the poorer coverage of the other regions, often associated with larger errors, at high latitudes, mainly resulting from persistent clouds or the difficulty to identify the presence of ice (e.g. O'Carroll et al., 2019). Given the equator crossing time drifting of Metop-A since August 2017, due to the interruption of the inclination correction, the monthly SSTs retrieved from Metop-B are used instead of those provided by Metop-A from January 2014, in order to keep the same local time of observation for the whole series. January 2014 was chosen arbitrarily, but differences are small when another date is used.

Figure 10 displays the IASI 60°S-60°N average of the monthly 1°x1° SST anomalies and compares them with the anomalies for the same region similarly calculated from other SST products, namely: (1) The Atmospheric Infrared Sounder (AIRS) daily 1°x1° night-time skin SST AIRS3STD.007 (Olsen et al., 2017) available on https://acdisc.gesdisc.eosdis.nasa.gov/ (only sea has been used). (2) The 0.25°x0.25° monthly Operational SST and Sea Ice Analysis (OSTIA) system (Donlon et al., 2012), a merged multi-sensor L4 Foundation SST product based on AVHRR, AVHRR_GAC, AVHRR_LAC, IASI, SEVIRI, TMI, GOES Imager, SSMIS, SSM/I available at https://marine.copernicus.eu/. (3) The Hadley Centre SST data set (HadSST3), a composite SST series that assimilates data from different platforms (ships and

buoys from ICOADS) (Kennedy et al., 2011) available at https://www.metoffice.gov.uk/. Since, for HadSST3, only the anomaly is provided, this product was directly used after applying a correction of -0.455 K to the original dataset, calculated with the 1961-1991 period as reference, in order to adjust the reference to the studied IASI period (this correction corresponds to the average HadSST3 anomaly over the 2008-2020 period). (4) ERA5. Note that OSTIA is used as boundary condition in ERA5 (Hersbach et al., 2020). The linear time dependence least square fits of the various anomaly time series are also plotted in Figure 10.

The different products are in good agreement, with temporal correlations of 0.91 between IASI and AIRS, of 0.96 between IASI and OSTIA, and of 0.89 between IASI and HadSST3. Note that the OSTIA and ERA5 results are superimposed, showing how SST products can be interconnected. All the results in Figure 10 agreed on the continuous global warming of the ocean surfaces since 2008, even if the increase within the studied 13 years is slightly higher for IASI (+0.33 +/-0.04 K/decade) and AIRS (+0.32 +/-0.04 K/decade), than for OSTIA and ERA5 (+0.25 +/-0.03 K/decade) or HadSST3 (+0.26 +/-0.04 K/decade). It should be emphasized that the IASI and AIRS results are both *fully* independent of in-situ buoys measurements, which is not the case for the others. Using only Metop-A for the anomaly time series would give an increase of +0.02 K/decade of the trend when compared to what is obtained by combining Metop-A and –B. This difference is consistent with a slight increase of the observed temperature which may be due to the Metop-A drift toward earlier observing hours. The large inter-annual variations, principally driven by the El Nino South Oscillation (ENSO), are also consistent from one product to the other. In 2009-2010, 2015-2016 and 2019-2020 El Nino warm phases are indeed observed in all the products, 2016 being the hottest year of the studied period, as are the 2008, 2011-2012 and 2017 and 2018-2019 La Nina cold phases. Temperature oscillations at short time scales are more or less important depending on the considered SST data set. This variability is expected given the differences in the products (spatial coverage, kind of observations, retrieval techniques, etc…). Note that the results in Figure 10 are very consistent with those displayed in Fig. 1 of (Hausfather et al., 2017) where a more detailed analysis of the results can be found.

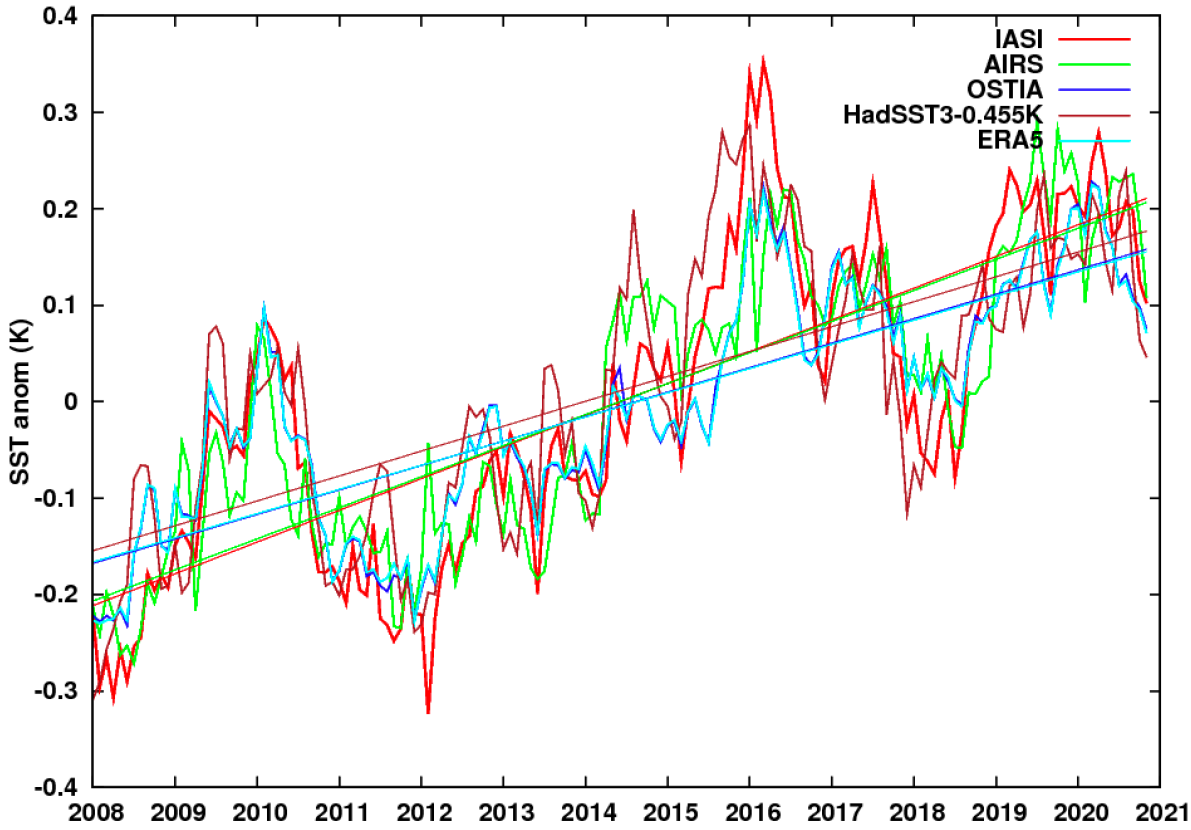

Figure 10 : Monthly mean SST anomalies calculated from the monthly averages over the period 2008-2020 for IASI, AIRS and OSTIA. For HadSST3 a correction of -0.455 K was made on the original time series calculated with the 1961-1991 period to adapt the reference to the IASI period. The straight lines represent to the linear evolutions with time least square fitted to each anomaly time series.

This section demonstrates the capability of IASI to correctly observe and quantify year-to-year SST variations, as well as to capture the global warming of the last 15 years. It must be emphasized that such an *independent* product is important to corroborate other observations, which often more or less use the same external datasets, such as the buoys or ships measurements. Here, the time series obtained from the two independent (IASI and AIRS) satellite products highlight a warming slightly more important than do the products based on buoys measurements. This difference has already been observed for AIRS data over the 2003-2017 period (Susskind et al., 2019), although it was smaller than in the present study. These very preliminary results must however be treated with caution given the difficulty to estimate short-term trends given the large inter-annual variability of the time series.

5 Conclusion

In this study a fully physically-based model is described and used for retrievals of night-time sea surface temperatures (SSTs) from spectra provided by the IASI instrument. The ultimate objective is to provide an accurate and homogeneous dataset, *totally* independent of in-situ measurements or models, over long time periods well suited for climate studies. SSTs have been retrieved, at the IASI spot resolution (clear sky), using radiances collected from the three Metop platforms: Metop-A from June 2007, Metop-B from February 2013 and Metop-C from July 2019. The quality of the retrieval has been assessed through comparisons with bulk temperatures measured from collocated drifting buoys. The analysis of the resulting "satellite skin" minus "buoys bulk" temperature differences, which depend not only on the error on the temperature retrieval or in-situ measurement, but also on the energy exchanges between the

atmosphere and ocean, was made using a physically-based modeling of the "cool-skin effect". The results obtained are very encouraging and the main achievements are the following.

It has been shown that long wavelengths (8-12 μm spectral region) are too sensitive to the atmospheric absorption to be reliably used in the fully physically-based retrieval algorithm retained in the present study. Indeed, when using this spectral domain, a very accurate (and rarely reached) knowledge of the atmospheric state is required together with precise spectroscopic information on H_2O absorption (which is not the case so far for the water-vapor continua), in order to prevent significant errors in case of the humid atmospheres that can be found in the Tropics. In contrast, we demonstrate that wavelengths shorter than 4 μm are much better suited, given their high sensitivity to surface temperature variations and their lower sensitivity to the assumed known spectroscopic and atmospheric-state parameters. The use of this spectral region with IASI can appear challenging, given the high radiometric noise below 4 μm, but this difficulty is overpassed by the use of 185 channels between 2550 cm^{-1} and 2760 cm^{-1} (3.9 μm–3.6 μm). For these wavelengths, the direct comparison of the IASI-retrieved skin temperatures with in-situ bulk temperatures measured from collocated buoys is very consistent (regardless of the wind speed, air-sea temperature difference and TPW) with the theoretical predictions of (Fairall et al., 1996), as well as with the empirical relationships of (Donlon et al., 2002; Zhang et al., 2020). Moreover, the analysis of this difference as a function of the atmospheric water content shows no strong relationship that would indicate a too large sensitivity to errors made on the water profile or the spectroscopy. This implies that our retrievals provide accurate estimations of the sea surface skin temperature, even when very humid atmospheres are involved, which is not always the case, as noted for AVHRR (Merchant et al., 2009), MODIS (Kilpatrick et al., 2015 and this study) or AATSR (Embury et al., 2012).

In order to further quantify the accuracy, precision and stability of the IASI restitutions, the skin temperatures retrieved from IASI spectra near 3.8 μm have been converted to bulk-equivalent temperatures using the parametrization of (Fairall et al., 1996) and the ERA5 heat flux. Median and robust standard deviation (RSD) for the difference between these temperatures and in-situ collocated measurements have then been evaluated for Metop-A (Metop-B) from January 2008 (February 2013) to June 2020. The results obtained for Metop-A and Metop-B are very accurate and consistent, with medians of -0.025 K and -0.015 K and RSDs of 0.256 K and 0.244 K, respectively. These demonstrated accuracies (biases) thus meet the requirement for climate studies (better than 0.1 K) defined in (Ohring et al., 2005). Note that the RSD is of the order of the buoys data precision of 0.21 K (Xu and Ignatov, 2016), implying a precision for the IASI retrieval better than this value. Finally, the variations of the median and RSD through time have been investigated, showing great stabilities: The trend of the RSD is lower than 0.5 mK/year and smaller than the 95% confidence interval, and the worldwide variation of the median with time is 4.5 mK/year. This last value is only very slightly above the limit of 4 mK/year prescribed in (Ohring et al., 2005). However, within the -20°S-20°N region, this variation is reduced to 2.4 mK/year, which confirms the high stability of the IASI SST time series (and indirectly the high radiometric stability of the instrument).

Finally, the consistency between the data provided by IASI onboard the three Metop (A, B and C) satellites has also been checked on a worldwide scale by considering the monthly averaged SST over 1°x1° grids. Biases are lower than 0.02 K and the standard deviation of about 0.3 K is of the order of the monthly variation of the SST for a given instrument and for a given grid cell. This value principally reflects the fact that the resulting monthly averaged SST for one satellite does not correspond to the same days of observation as those of the other satellites. This high consistency between the data provided (and retrieved from) the three instruments opens the possibility to retrieve long time SST series without the need for any radiative correction to the newest instrument data to be consistent with those provided by the older one(s). This is demonstrated by analyzing the 60°S-60°N monthly-averaged retrieved SST

anomaly from 2008 to 2020 obtained by a combination of Metop-A and Metop-B observations and comparing them with other SST results provided by AIRS, OSTIA, ERA5 and HadSST3. The fact that IASI indeed enables to detect short- and long-term trends as well as inter-annual variability, opens promising perspectives for climate studies.

Declaration of Competing Interest :
The authors declare that they have no known competing financial interests or personal relationships that could have appeared to influence the work reported in this paper.

Acknowledgments : This work has been supported in part by CNRS, CNES and Ecole polytechnique. We particularly acknowledge the EUMETSAT and EUMETCast service for providing IASI L1C data and the Aeris data infrastructure for providing access to the IASI data via ESPRI (https://www.aeris-data.fr). Calculations were performed using the resources of the IPSL data and computing centre ClimServ. We thank E.G. Mlawer (for providing information on the water vapor continua uncertainies). OSTIA data were provided by GHRSST, Met Office and CMEMS.

Appendices:

A1. Sensitivity of the retrieved SST to a change of the water vapor profile, of the surface emissivity or of the temperature profile.

Figure A1 displays the variations of the SST retrieved, for all collocations with Metop-A in 2016, from the different spectral windows of IASI spectra when the water profile is increased by +10 %, when the surface emissivity from (Masuda et al., 1988) is increased by +0.001, or when the temperature profile is changed by +1 K. In all cases, the input (measured) brightness temperatures used remain unchanged.

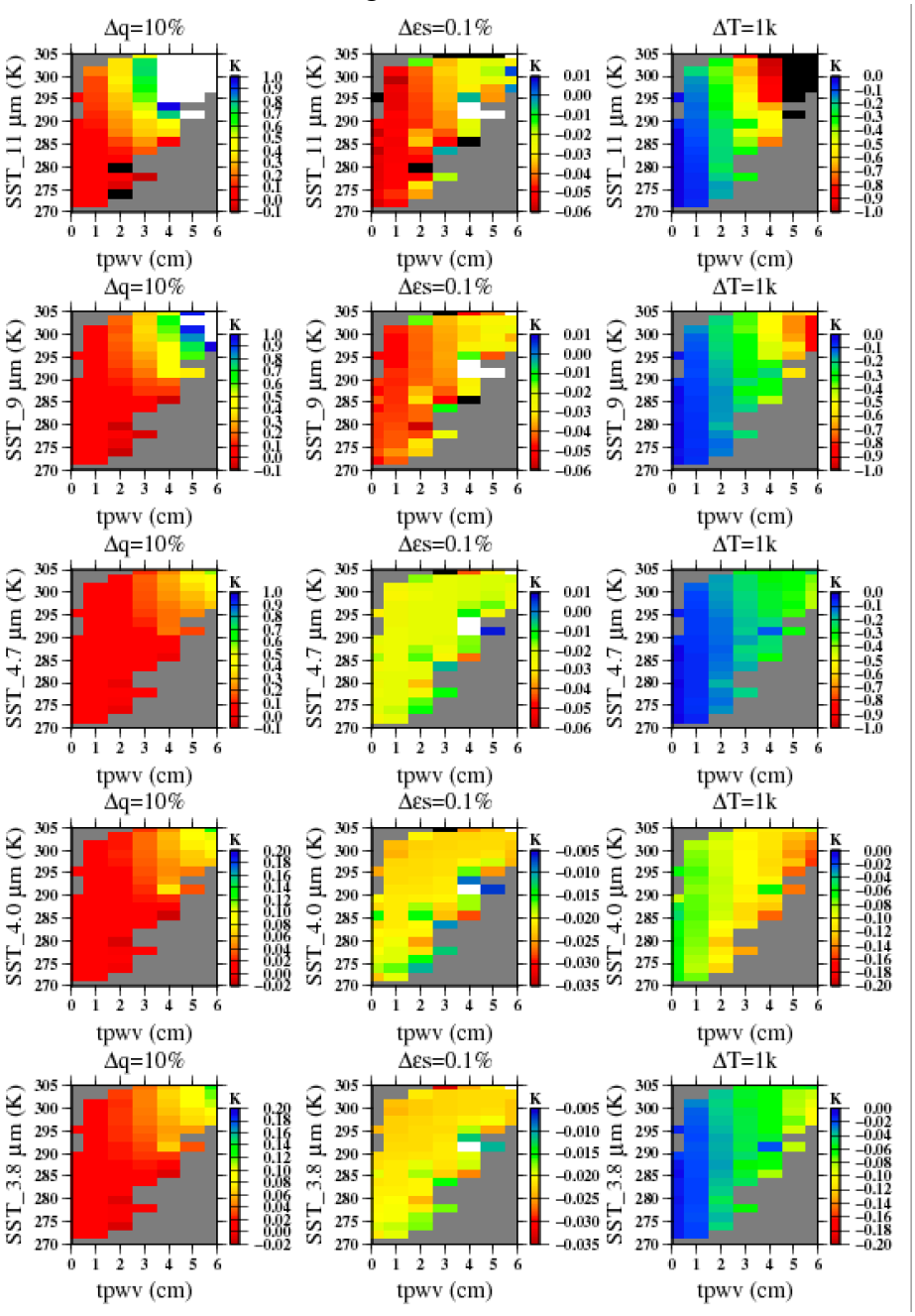

Figure A1: Sensitivity of the retrieved SSTs to atmospheric and surface parameters. Left: for a variation Δq of +10 % of the TPW; middle: for a variation Δεs of +0.001 of the surface emissivity; right: for a variation ΔT of +1 K of the temperature profile. Each line corresponds to one of the 5 spectral regions analyzed, i.e. from top down: 11, 9.0, 4.7, 4.0 and 3.8 µm. The white (resp. black) color denotes values larger (resp. smaller) than the color scale maximum (resp. minimum). Note that the scales of variation of the SSTs retrieved at 11.0, 9.0 and 4.7 µm are different from those used for SSTs retrieved at 4.0 and 3.8 µm.

As obvious from this plot, the long wavelengths are significantly more impacted than the shortest ones. This is particularly the case for the influence of the TPW, a finding strongly in favor of the use of the high frequency spectral region of IASI spectra for SST retrievals, particularly for very humid (tropical) atmospheres.

A2. Sensitivity of the retrieved SSTs to the water vapor continua

Figure A2 displays the variations of the SST retrieved, for all collocations with Metop-A in 2016, from the different spectral windows of IASI spectra when the water vapor self-continuum or the foreign-continuum from (Mlawer et al., 2012) is changed by +10 %. In all case, the input (measured) brightness temperatures used remain unchanged.

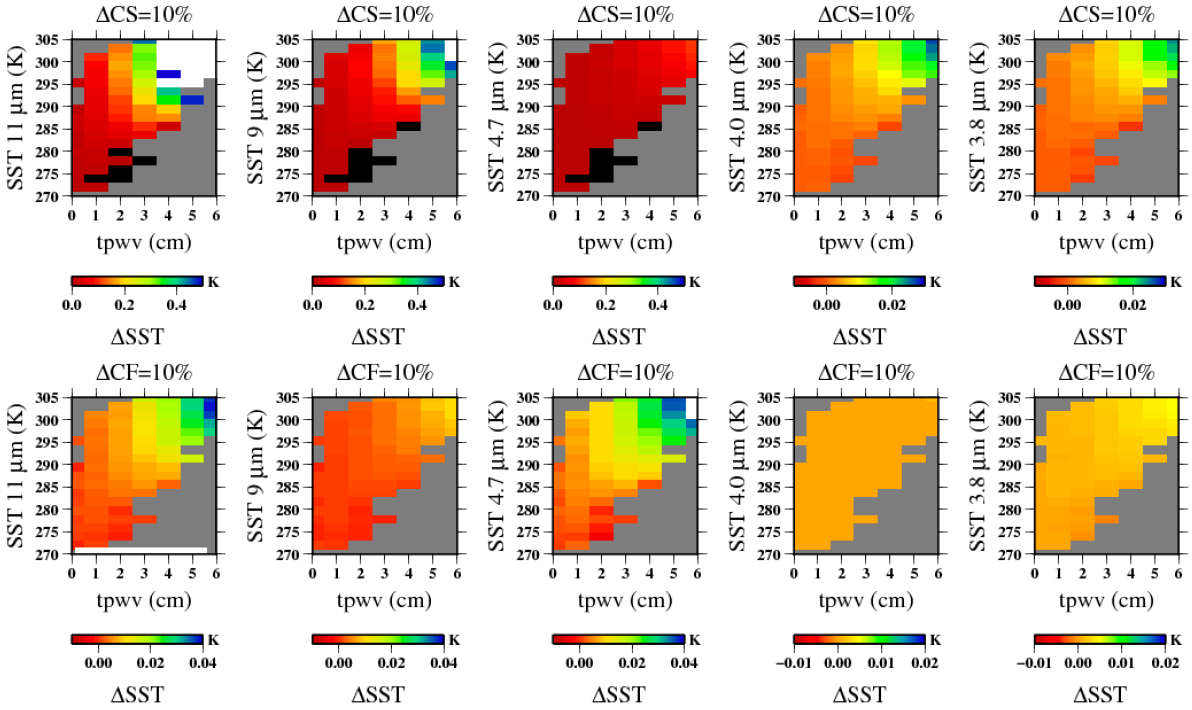

Figure A2: Same as Figure A1, but here for the sensitivity of the retrieved SSTs to changes in the self (ΔCS) and foreign (ΔCF) water vapor continua. Top: for a variation of +10 % of the self-continuum; bottom: for a variation of +10 % of the foreign continuum. Each column corresponds to one of the 5 spectral regions (note that the associated scales for the variations of the SSTs induced by changes of the self and foreign continua are different).

As obvious from this plot, the long wavelengths are significantly more impacted than the shortest ones by uncertainties on the spectroscopic knowledge of the continua (particularly for the self continuum). This effect, which increases with the TPW, further amplifies the conclusion of Appendix A1 that one should preferably use the highest frequency spectral region of IASI spectra for SST retrievals, particularly for very humid (tropical) atmospheres.

References

Alappattu, D.P., Wang, Q., Yamaguchi, R., Lind, R.J., Reynolds, M., Christman, A.J., 2017. Warm layer and cool skin corrections for bulk water temperature measurements for air-sea interaction studies. J. Geophys. Res. Ocean. 122, 6470–6481. doi:10.1002/2017JC012688

August, T., Klaes, D., Schï ussel, P., Hultberg, T., Crapeau, M., Arriaga, A., Coppens, D., Munro, R., Calbet, X., Schlüssel, P., Hultberg, T., Crapeau, M., Arriaga, A., O'Carroll, A., Coppens, D., Munro, R., Calbet, X., 2012. IASI on Metop-A: Operational Level 2 retrievals after five years in orbit. J. Quant. Spectrosc. Radiat. Transf. 113, 1340–1371. doi:10.1016/j.jqsrt.2012.02.028

Berry, D.I., Corlett, G.K., Embury, O., Merchant, C.J., 2018. Stability assessment of the (A)ATSR sea surface temperature climate dataset from the European Space Agency Climate Change Initiative. Remote Sens. 10, 126. doi:10.3390/rs10010126

Blumstein, D., Chalon, G., Carlier, T., Buil, C., Hebert, P., Maciaszek, T., Ponce, G., Phulpin, T., Tournier, B., Simeoni, D., Astruc, P., Clauss, A., Kayal, G., Jegou, R., 2004. IASI instrument: technical overview and measured performances, in: Strojnik, M. (Ed.), Infrared Spaceborne Remote Sensing XII. SPIE, pp. 196–207. doi:10.1117/12.560907

Bojinski, S., Verstraete, M., Peterson, T.C., Richter, C., Simmons, A., Zemp, M., 2014. The concept of essential climate variables in support of climate research, applications, and policy. Bull. Am. Meteorol. Soc. 95, 1431–1443. doi:10.1175/BAMS-D-13-00047.1

Capelle, V., Chédin, A., Péquignot, E., Schlüssel, P., Newman, S.M., Scott, N.A., 2012. Infrared continental surface emissivity spectra and skin temperature retrieved from IASI observations over the tropics. J. Appl. Meteorol. Climatol. 51, 1164–1179. doi:10.1175/JAMC-D-11-0145.1

Capelle, V., Chédin, A., Pondrom, M., Crevoisier, C., Armante, R., Crepeau, L., Scott, N.A., 2018. Infrared dust aerosol optical depth retrieved daily from IASI and comparison with AERONET over the period 2007–2016. Remote Sens. Environ. 206, 15–32. doi:10.1016/J.RSE.2017.12.008

Castro, S.L., Wick, G.A., Emery, W.J., 2003. Further refinements to models for the bulk-skin sea surface temperature difference. J. Geophys. Res. 108, 3377. doi:10.1029/2002JC001641

Chedin, A., Scott, N.A., Wahiche, C., Moulinier, P., 1985. The improved initialisation inversion method: A high-resolution physical method for temperature retrievals from the TIROS-N series. J. Clim. Appl. Meteorol. doi:10.1175/1520-0450(1985)024<0128:TIIIMA>2.0.CO;2

Chevallier, F.C., Chéruy, F., Scott, N.A., Chédin, A., 1998. A Neural Network Approach for a Fast and Accurate Computation of a Longwave Radiative Budget. J. Appl. Meteorol. 37, 1385–1397. doi:10.1175/1520-0450(1998)037<1385:annafa>2.0.co;2

Donlon, C., Robinson, I.S., Reynolds, M., Wimmer, W., Fisher, G., Edwards, R., Nightingale, T.J., 2008. An Infrared Sea Surface Temperature Autonomous Radiometer (ISAR) for Deployment aboard Volunteer Observing Ships (VOS). Am. Meteorol. Soc. 25, 93–113. doi:10.1175/2007JTECHO505.1

Donlon, C.J., Martin, M., Stark, J., Roberts-Jones, J., Fiedler, E., Wimmer, W., 2012. The Operational Sea Surface Temperature and Sea Ice Analysis (OSTIA) system. Remote Sens. Environ. 116, 140–158. doi:10.1016/j.rse.2010.10.017

Donlon, C.J., Minnett, P.J., Gentemann, C., Nightingale, T.J., Barton, I.J., Ward, B., Murray, M.J., 2002. Toward improved validation of satellite sea surface skin temperature measurements for climate research. J.

Clim. 15, 353–369. doi:10.1175/1520-0442(2002)015<0353:TIVOSS>2.0.CO;2

Dyer, R., Righetti, P.L., Vera, C., Vey, S., 2018. Metop-a lifetime extension – surviving on a drifting LTAN, in: 15th International Conference on Space Operations, 2018. the American Institute of Aeronautics and Astronautics, Inc., Marseille, France. doi:10.2514/6.2018-2439

Embury, O., Merchant, C., Good, S., 2019. Copernicus Climate Change Service Product Quality Assessment Report: Sea Surface Temperature, contract 2018/C3S_312b_Lot3_CLS/SC2 [WWW Document]. URL http://datastore.copernicus-climate.eu/documents/satellite-sea-surface-temperature/v2.0/D2.SST.2-v2.1_PQAR_of_v2SST_products_v3.1_APPROVED_Ver1.pdf

Embury, O., Merchant, C.J., Corlett, G.K., 2012. A reprocessing for climate of sea surface temperature from the along-track scanning radiometers: Initial validation, accounting for skin and diurnal variability effects. Remote Sens. Environ. 116, 62–78. doi:10.1016/J.RSE.2011.02.028

Emery, W.J., Castro, S., Wick, G.A., Schluessel, P., Donlon, C., 2001. Estimating sea surface temperature from infrared satellite and in situ temperature data. Bull. Am. Meteorol. Soc. 82, 2773–2785. doi:10.1175/1520-0477(2001)082<2773:ESSTFI>2.3.CO;2

EUMETSAT, 2014. GSICS Traceability Statement for IASI and AIRS, Doc. No. EUM/MET/TEN/11/0157 [WWW Document]. URL http://www.eumetsat.int

Fairall, C., Bradley, E.F., Godfrey, J.S., Wick, G.A., Edson, J.B., Young, G.S., 1996. Cool-skin and warm-layer effects on sea surface temperature. J. Geophys. Res. Atmos. 101, 1295–1308. doi:DOI: 10.1029/95JC03190

Hamed, K.H., 2009. Enhancing the effectiveness of prewhitening in trend analysis of hydrologic data. J. Hydrol. 368, 143–155. doi:10.1016/j.jhydrol.2009.01.040

Hartmann, J.-M., Armante, R., Toon, G.C., Scott, N., Tran, H., Crevoisier, C., Chédin, A., Capelle, V., 2018. Indirect Influence of Humidity on Atmospheric Spectra Near 4 μm. Geophys. Res. Lett. doi:10.1029/2018GL079582

Hausfather, Z., Cowtan, K., Clarke, D.C., Jacobs, P., Richardson, M., Rohde, R., 2017. Assessing recent warming using instrumentally homogeneous sea surface temperature records. Sci. Adv. 3, 1601207. doi:10.1126/sciadv.1601207

Hersbach, H., Bell, B., Berrisford, P., Biavati, G., Horányi, A., Muñoz Sabater, J., Nicolas, J., Peubey, C., Radu, R., Rozum, I., Schepers, D., Simmons, A., Soci, C., Dee, D., Thépaut, J.-N., 2018. ERA5 hourly data on single levels from 1979 to present. Copernicus Climate Change Service (C3S) Climate Data Store (CDS). (Accessed on < 01-09-2020 >), available on https://cds.climate.copernicus.eu/ [WWW Document]. doi:10.24381/cds.adbb2d47

Hersbach, H., Bell, B., Berrisford, P., Hirahara, S., Horányi, A., Muñoz-Sabater, J., Nicolas, J., Peubey, C., Radu, R., Schepers, D., Simmons, A., Soci, C., Abdalla, S., Abellan, X., Balsamo, G., Bechtold, P., Biavati, G., Bidlot, J., Bonavita, M., De Chiara, G., Dahlgren, P., Dee, D., Diamantakis, M., Dragani, R., Flemming, J., Forbes, R., Fuentes, M., Geer, A., Haimberger, L., Healy, S., Hogan, R.J., Hólm, E., Janisková, M., Keeley, S., Laloyaux, P., Lopez, P., Lupu, C., Radnoti, G., de Rosnay, P., Rozum, I., Vamborg, F., Villaume, S., Thépaut, J.N., 2020. The ERA5 global reanalysis. Q. J. R. Meteorol. Soc. 146, 1999–2049. doi:10.1002/qj.3803

Hewison, T.J., Wu, X., Yu, F., Tahara, Y., Hu, X., Kim, D., Koenig, M., 2013. GSICS inter-calibration of

infrared channels of geostationary imagers using metop/IASI. IEEE Trans. Geosci. Remote Sens. 51, 1160–1170. doi:10.1109/TGRS.2013.2238544

Hilton, F., Armante, R., August, T., Barnet, C., Bouchard, A., Camy-Peyret, C., Capelle, V., Clarisse, L., Clerbaux, C., Coheur, P.F., Collard, A., Crevoisier, C., Dufour, G., Edwards, D., Faijan, F., Fourrié, N., Gambacorta, A., Goldberg, M., Guidard, V., Hurtmans, D., Illingworth, S., Jacquinet-Husson, N., Kerzenmacher, T., Klaes, D., Lavanant, L., Masiello, G., Matricardi, M., McNally, A., Newman, S., Pavelin, E., Payan, S., Péquignot, E., Peyridieu, S., Phulpin, T., Remedios, J., Schlüssel, P., Serio, C., Strow, L., Stubenrauch, C., Taylor, J., Tobin, D., Wolf, W., Zhou, D., 2012. Hyperspectral earth observation from IASI. Bull. Am. Meteorol. Soc. 93, 347–370. doi:10.1175/BAMS-D-11-00027.1

Horrocks, L.A., Candy, B., Nightingale, T.J., Saunders, R.W., O'Carroll, A., Harris, A.R., 2003. Parameterizations of the ocean skin effect and implications for satellite-based measurement of sea-surface temperature. J. Geophys. Res. Ocean. 108. doi:10.1029/2002jc001503

Jacquinet-Husson, N., Armante, R., Scott, N.A., Chédin, A., Crépeau, L., Boutammine, C., Bouhdaoui, A., Crevoisier, C., Capelle, V., Boonne, C., Poulet-Crovisier, N., Barbe, A., Chris Benner, D., Boudon, V., Brown, L.R., Buldyreva, J., Campargue, A., Coudert, L.H., Devi, V.M., Down, M.J., Drouin, B.J., Fayt, A., Fittschen, C., Flaud, J.M., Gamache, R.R., Harrison, J.J., Hill, C., Hodnebrog, Hu, S.M., Jacquemart, D., Jolly, A., Jiménez, E., Lavrentieva, N.N., Liu, A.W., Lodi, L., Lyulin, O.M., Massie, S.T., Mikhailenko, S., Müller, H.S.P., Naumenko, O. V., Nikitin, A., Nielsen, C.J., Orphal, J., Perevalov, V.I., Perrin, A., Polovtseva, E., Predoi-Cross, A., Rotger, M., Ruth, A.A., Yu, S.S., Sung, K., Tashkun, S.A., Tennyson, J., Tyuterev, V.G., Vander Auwera, J., Voronin, B.A., Makie, A., 2016. The 2015 edition of the GEISA spectroscopic database. J. Mol. Spectrosc. 327, 31–72. doi:10.1016/j.jms.2016.06.007

Kennedy, J.J., Rayner, N.A., Smith, R.O., Parker, D.E., Saunby, M., 2011. Reassessing biases and other uncertainties in sea surface temperature observations measured in situ since 1850: 1. Measurement and sampling uncertainties. J. Geophys. Res. Atmos. 116. doi:10.1029/2010JD015218

Kilpatrick, K.A., Baker-Yeboah, S., 2016. Climate Algorithm Theoretical Basis Document (C-ATBD), Sea Surface Temperature - Pathfinder [WWW Document]. URL ftp://ftp.ncdc.noaa.gov/pub/data/sds/cdr/docs/pfsst-algorithm-description.pdf

Kilpatrick, K.A., Podestá, G., Walsh, S., Williams, E., Halliwell, V., Szczodrak, M., Brown, O.B., Minnett, P.J., Evans, R., 2015. A decade of sea surface temperature from MODIS. Remote Sens. Environ. 165, 27–41. doi:10.1016/j.rse.2015.04.023

Kilpatrick, K.A., Podestá, G.P., Evans, R., 2001. Overview of the NOAA/NASA advanced very high resolution radiometer Pathfinder algorithm for sea surface temperature and associated matchup database. J. Geophys. Res. Ocean. 106, 9179–9197. doi:10.1029/1999jc000065

Liu, W.T., Katsaros, K.B., Businger, J.A., 1979. Bulk Parameterization of Air-Sea Exchanges of Heat and Water Vapor Including the Molecular Constraints at the Interface. J. Atmos. Sci. 36, 1722–1735. doi:10.1175/1520-0469(1979)036<1722:BPOASE>2.0.CO;2

Masuda, K., Takashima, T., Takayama, Y., 1988. Emissivity of Pure and Sea Waters for the Model Sea Surface in the Infrared Window Regions. Remote Sens. Environ. 24, 313–329. doi:10.1016/0034-4257(88)90032-6

Merchant, C.J., Embury, O., Bulgin, C.E., Block, T., Corlett, G.K., Fiedler, E., Good, S.A., Mittaz, J., Rayner, N.A., Berry, D., Eastwood, S., Taylor, M., Tsushima, Y., Waterfall, A., Wilson, R., Donlon, C., 2019.

Satellite-based time-series of sea-surface temperature since 1981 for climate applications. Sci. data 6, 223. doi:10.1038/s41597-019-0236-x

Merchant, C.J., Embury, O., Rayner, N.A., Berry, D.I., Corlett, G.K., Lean, K., Veal, K.L., Kent, E.C., Llewellyn-Jones, D.T., Remedios, J.J., Saunders, R., 2012. A 20 year independent record of sea surface temperature for climate from Along-Track Scanning Radiometers. J. Geophys. Res. Ocean. 117, 1–18. doi:10.1029/2012JC008400

Merchant, C.J., Embury, O., Roberts-Jones, J., Fiedler, E., Bulgin, C.E., Corlett, G.K., Good, S., McLaren, A., Rayner, N., Morak-Bozzo, S., Donlon, C., Roberts-Jones, J., Fiedler, E., Bulgin, C.E., Corlett, G.K., Good, S., McLaren, A., Rayner, N., Morak-Bozzo, S., Donlon, C., 2014. Sea surface temperature datasets for climate applications from Phase 1 of the European Space Agency Climate Change Initiative (SST CCI). Geosci. Data J. 1, 179–191. doi:10.1002/gdj3.20

Merchant, C.J., Harris, A.R., Roquet, H., Le Borgne, P., 2009. Retrieval characteristics of non-linear sea surface temperature from the Advanced Very High Resolution Radiometer. Geophys. Res. Lett. 36, 1–5. doi:10.1029/2009GL039843

Merchant, C.J., Llewellyn-Jones, D., Saunders, R.W., Rayner, N.A., Kent, E.C., Old, C.P., Berry, D., Birks, A.R., Blackmore, T., Corlett, G.K., Embury, O., Jay, V.L., Kennedy, J., Mutlow, C.T., Nightingale, T.J., O'Carroll, A.G., Pritchard, M.J., Remedios, J.J., Tett, S., 2008. Deriving a sea surface temperature record suitable for climate change research from the along-track scanning radiometers. Adv. Sp. Res. 41, 1–11. doi:10.1016/J.ASR.2007.07.041

Minnett, P.J., Alvera-Azcárate, A., Chin, T.M., Corlett, G.K., Gentemann, C.L., Karagali, I., Li, X., Marsouin, A., Marullo, S., Maturi, E., Santoleri, R., Saux Picart, S., Steele, M., Vazquez-Cuervo, J., 2019. Half a century of satellite remote sensing of sea-surface temperature. Remote Sens. Environ. 233, 111366. doi:10.1016/j.rse.2019.111366

Minnett, P.J., Corlett, G.K., 2012. A pathway to generating Climate Data Records of sea-surface temperature from satellite measurements. Deep. Res. Part II Top. Stud. Oceanogr. 77–80, 44–51. doi:10.1016/j.dsr2.2012.04.003

Minnett, P.J., Knuteson, R.O., Best, F.A., Osborne, B.J., Hanafin, J.A., Brown, O.B., 2001. The marine-atmospheric emitted radiance interferometer: A high-accuracy, seagoing infrared spectroradiometer. J. Atmos. Ocean. Technol. 18, 994–1013. doi:10.1175/1520-0426(2001)018<0994:TMAERI>2.0.CO;2

Minnett, P.J., Smith, M., Ward, B., 2011. Measurements of the oceanic thermal skin effect. Deep. Res. Part II 58, 861–868. doi:10.1016/j.dsr2.2010.10.024

Mlawer, 2020. Private communication.

Mlawer, E.J., Payne, V.H., Moncet, J.-L., Delamere, J.S., Alvarado, M.J., Tobin, D.C., 2012. Development and recent evaluation of the MT_CKD model of continuum absorption. Trans. R. Soc. A 370, 2520–2556. doi:10.1098/rsta.2011.0295

Nayar, K.G., Sharqawy, M.H., Banchik, L.D., Lienhard V, J.H., 2016. Thermophysical properties of seawater: A review and new correlations that include pressure dependence. Desalination 390, 1–24. doi:10.1016/J.DESAL.2016.02.024

Newman, S.M., Smith, J.A., Glew, M.D., Rogers, S.M., Taylor, J.P., 2005. Temperature and salinity dependence of sea surface emissivity in the thermal infrared. Q. J. R. Meteorol. Soc. 131, 2539–2557.

doi:10.1256/qj.04.150

O'Carroll, A.G., Armstrong, E.M., Beggs, H., Bouali, M., Casey, K.S., Corlett, G.K., Dash, P., Donlon, C., Gentemann, C.L., Høyer, J.L., Ignatov, A., Kabobah, K., Kachi, M., Kurihara, Y., Karagali, I., Maturi, E., Merchant, C.J., Marullo, S., Minnett, P., Pennybacker, M., Ramakrishnan, B., Ramsankaran, R.A.A.J., Santoleri, R., Sunder, S., Picart, S.S., Vázquez-Cuervo, J., Wimmer, W., 2019. Observational needs of sea surface temperature. Front. Mar. Sci. 6. doi:10.3389/fmars.2019.00420

O'Carroll, A.G., August, T., Le Borgne, P., Marsouin, A., 2012. The accuracy of SST retrievals from Metop-A IASI and AVHRR using the EUMETSAT OSI-SAF matchup dataset. Remote Sens. Environ. 126, 184–194. doi:10.1016/j.rse.2012.08.006

O'Carroll, A.G., Eyre, J.R., Saunders, R.W., O'carroll, A.G., Eyre, J.R., Saunders, R.W., 2008. Three-Way Error Analysis between AATSR, AMSR-E, and In Situ Sea Surface Temperature Observations. J. Atmos. Ocean. Technol. 25, 1197–1207. doi:10.1175/2007JTECHO542.1

Ohring, G., Wielicki, B., Spencer, R., Emery, B., Datla, R., 2005. Satellite instrument calibration for measuring global climate change: Report of a workshop. Bull. Am. Meteorol. Soc. 86, 1303–1313. doi:10.1175/BAMS-86-9-1303

Olsen, E.T., Aumann, H., Broberg, S., Chen, L., Elliott, D., Fetzer, E., Fishbein, E., Friedman, S., Gaiser, S., Granger, S., Kapoor, M., Lambrigtsen, B., Lee, S., Licata, S., Manning, E., Blaisdell, J., Susskind, J., 2017. AIRS / AMSU / HSB Version 6.0 Data Release User Guide Edited by : [WWW Document]. Jet Propul Lab. URL https://docserver.gesdisc.eosdis.nasa.gov/repository/Mission/AIRS/3.3_ScienceDataProductDocumentation/3.3.4_ProductGenerationAlgorithms/V6_Data_Release_User_Guide.pdf

Péquignot, E., Chédin, A., Scott, N.A., 2008. Infrared continental surface emissivity spectra retrieved from AIRS hyperspectral sensor. J. Appl. Meteorol. Climatol. 47, 1619–1633. doi:10.1175/2007JAMC1773.1

Pinkley, L.W., Sethna, P.P., Williams, D., 1977. Optical constants of water in the infrared: Influence of temperature*. J. Opt. Soc. Am. 67, 494. doi:10.1364/josa.67.000494

Reynolds, R.W., Smith, T.M., Liu, C., Chelton, D.B., Casey, K.S., Schlax, M.G., 2007. Daily high-resolution-blended analyses for sea surface temperature. J. Clim. 20, 5473–5496. doi:10.1175/2007JCLI1824.1

Rousseeuw, P.J., Hubert, M., 2011. Robust statistics for outlier detection. Wiley Interdiscip. Rev. Data Min. Knowl. Discov. 1, 73–79. doi:10.1002/widm.2

Saunders, P.M., 1967. The Temperature at the Ocean-Air Interface. J. Atmos. Sci. 24, 269–273. doi:10.1175/1520-0469(1967)024<0269:ttatoa>2.0.co;2

Schluessel, P., Emery, W.J., Grassl, H., Mammen, T., 1990. On the Bulk-Skin Temperature Difference and Its Impact on Satellite Remote Sensing of Sea Surface Temperature. J. Geophys. Res. 95, 13341–13354. doi:10.1029/JC095iC08p13341

Scott, N.A., Chédin, A., 1981. A Fast Line-by-Line Method for Atmospheric Absorption Computations: The Automatized Atmospheric Absorption Atlas. J. Appl. Meteorol. 20, 802–812. doi:10.1175/1520-0450(1981)020<0802:AFLBLM>2.0.CO;2

Sharqawy, M.H., Lienhard V, J.H., Zubair, S.M., 2010. Thermophysical properties of seawater: a review of existing correlations and data. Desalin. Water Treat. 16, 354–380. doi:10.5004/dwt.2010.1079

Soloviev, A. V., Schlüssel, P., 1994. Parameterization of the cool skin of the ocean and of the air-ocean gas

transfer on the basis of modeling surface renewal. J. Phys. Oceanogr. 24, 1339–1346. doi:10.1175/1520-0485(1994)024<1339:POTCSO>2.0.CO;2

Susskind, J., Schmidt, G.A., Lee, J.N., Iredell, L., 2019. Recent global warming as confirmed by AIRS. Environ. Res. Lett. 14. doi:10.1088/1748-9326/aafd4e

Tsamalis, C., Saunders, R., 2018. Quality assessment of sea surface temperature from ATSRs of the climate change initiative (Phase 1). Remote Sens. 10, 1–22. doi:10.3390/rs10040497

Turner, D.S., 2004. Systematic errors inherent in the current modeling of the reflected downward flux term used by remote sensing models. Appl. Opt. 43, 2369. doi:10.1364/ao.43.002369

Veal, K.L., Corlett, G.K., Ghent, D., Llewellyn-Jones, D.T., Remedios, J.J., 2013. A time series of mean global skin SST anomaly using data from ATSR-2 and AATSR. Remote Sens. Environ. 135, 64–76. doi:10.1016/j.rse.2013.03.028

Xu, F., Ignatov, A., 2016. Error characterization in iQuam SSTs using triple collocations with satellite measurements. Geophys. Res. Lett. 43, 10,826-10,834. doi:10.1002/2016GL070287

Xu, F., Ignatov, A., 2014. In situ SST Quality Monitor (iQuam). J. Atmos. Ocean. Technol. 31, 164–180. doi:10.1175/JTECH-D-13-00121.1

Zhang, H., Babanin, A. V., Liu, Q., Ignatov, A., 2019. Cool skin signals observed from Advanced Along-Track Scanning Radiometer (AATSR) and in situ SST measurements. Remote Sens. Environ. 226, 38–50. doi:10.1016/j.rse.2019.03.035

Zhang, H., Beggs, H., Ignatov, A., Babanin, A. V, 2020. Nighttime cool skin effect observed from infrared SST autonomous radiometer (ISAR) and depth temperatures. J. Atmos. Ocean. Technol. 37, 33–46. doi:10.1175/JTECH-D-19-0161.1

Zhang, Y., Zhang, X., 2012. Ocean haline skin layer and turbulent surface convections. J. Geophys. Res. Ocean. 117, 4017. doi:10.1029/2011JC007464